

Moments Based Spray Modelling

D. P. Jones* and A. P. Watkins

School of Engineering and Materials Science
Queen Mary, University of London, E1 4QD
dominic.jones@qmul.ac.uk, +44 (0) 20 7882 5512

School of Mechanical, Aerospace and Civil Engineering
University of Manchester, M60 1QD
paul.watkins@manchester.ac.uk, +44 (0) 161 306 3706

Abstract

This paper presents the current state of the spray modelling methodology, first presented in [4, 5], which uses the moments of the underlying droplet size distribution to characterize the spray. The paper presents the implementation of improved convection schemes for both the moments and their momentums, non-linear droplet velocity functions and the use of the Maximum Entropy formalism to recover the droplet density function. Three breakup models are compared, showing that the model in [8] is the most suitable. A thorough assessment of the broad range of algorithmic choices to simulate the spray model are presented. Based on these optimal choices the model is benchmarked against a wall impaction case from [16].

Keywords: spray, moments, modelling, wall impaction

1 Introduction

A computational spray model was presented in [5] which avoided the need to segregate the local droplet number distribution into parcels of identical droplets. Characteristics of the spray were instead obtained via the transportation of the third and fourth moments (μ_2 and μ_3) of the local droplet distribution and their moment-averaged momentums. From these moments, a special form of the Gamma distribution with one fixed parameter was used to recover the underlying local droplet size distribution in order for the computation of hydrodynamic forces acting on the droplets, such as inter-phase drag, droplet break-up and inter-droplet collisions. Evaluation of these forces required moments integrated over parts of the droplet size range, hence the transported moments alone without a distribution model did not suffice to close the spray model.

Whilst this novel spray model was shown to perform reasonably well, there were a number of outstanding issues still to be addressed. Two primary issues were analysed in [10], which were the limited capacity to represent a local underlying droplet size distribution based on one free parameter and the assumption that local droplets travel at the same speed.

*Corresponding Author

This paper attempts to address the remaining outstanding issues with the spray model presented in [5] and [12]. The most important of these was to make use of high order discretization techniques in both space and time. No attempt in the original spray model was made to use anything higher than first order approximations. One prominent consequence of this was the high degree of non-physical numerical diffusion of the spray in the radial plane immediately downstream of the injector. A second issue is the treatment of spray hydrodynamic terms. Their computation in an analytically integral manner in the original model effectively forced the assumption that local droplets travel at the same speed, to prevent the need of resorting to numerical integration. Whilst there are good reasons for this approach, in this paper integration is performed numerically to facilitate the use of more realistic local droplet velocity profiles.

Finally, the wall impaction model in [12], which was used to extend the spray model functionality is completely revised. The approach taken in that work was that the effect of the wall modified the behaviour of the impinging spray in the near-wall region. This is a reasonable approach to take when considering that the spray is being modelled as a continuum. However, the continuum is representing a discrete field of droplets which can interpenetrate. Such detail is lost in that approach. Here, the spray model proposed creates separately transported sprays for each new impaction regime, allowing for the more accurate representation of the spray upon impaction.

The paper is organised as follows: sections 2 - 4 place the method of moments in the context of spray representation and present the means of recovering underlying distributions. Following on from this, the recovery of moment-averaged properties, in particular the moment-averaged spray velocities, is outlined. From these two prerequisites the spray conservation equations are described. Sections 5 - 7 describe the hydrodynamics models which are implemented and the injection and wall impaction boundary conditions. This completes the spray model description.

The thesis of this paper is examined in sections 8 - 9: the testing of high order discretization methods, appropriateness of hydrodynamics models, droplet velocity profiles, moment closure methods, etc, to determine the most suitable modelling parameters. With these findings the spray model is set up to simulate as a benchmark the spray impaction case in [16].

2 Moments of a Continuous Distribution

The simplest definition of moments of a continuous distribution, $\phi(r)$, is the moments about its origin, defined as

$$\mu_i = \mu_0 \int_r \phi(r) r^i dr \quad (1)$$

whereby the first moment (when $i = 0$) simply returns the integral of the distribution. If the distribution is a probability density function, $\mu_0 = 1$; for a number density, the total number per unit volume; and for the volume density, the sum of the individual volumes per unit volume, etc.

Assuming the distribution to represent the range of (spherical) droplet sizes within a given volume, the first four moments of the distribution have physical interpretations (Table 1). In the case where the distribution is not a probability density, moments are often normalized by the constant, μ_0 , giving the normalized moments about the origin

$$\hat{\mu}_i = \frac{\mu_i}{\mu_0} \quad (2)$$

Moment ratios are of interest, providing definitions of different kinds of mean values based on the moments. This is defined as

$$r_{ji} = \left(\frac{\mu_j}{\mu_i} \right)^{\frac{1}{j-i}} \quad (3)$$

Table 1: Interpretation of moments

Quantity (per unit volume)	Moment Relation
Total number of droplets	μ_0
Sum of the radii	μ_1
Sum of the surface areas	$4\pi \mu_2$
Sum of the volumes	$\frac{4}{3}\pi \mu_3$

A moment ratio frequently cited in literature for characterising spray droplet size is the Sauter mean radius (SMR), r_{32} .

2.1 Distribution Construction Methods

In the spray model of [5], the distribution is not initially known and a means of determining the underlying probability density function is required given a finite set of its moments. If this given set of moments does not include the first moment, μ_0 , this has to be determined first.

This kind of problem is classified as an Inverse problem and is generally ill-posed; usually being deficient on one or more of the conditions of a well-posed problem (that of existence, uniqueness and stability) and as a result the computation of the solution is ill-conditioned [9].

A number of methods are available for prescribing the general form of a probability density function (PDF), such as assuming an a-priori form [26, 9], using polynomial fitting [9, 21] or the Maximum Entropy Formalism [1, 25]. Each method has different characteristics but none of them possesses all the qualities of a well-posed solution. For the spray model implemented here, the choice of distribution construction methods used are based on the findings in [10], i.e. the Maximum Entropy formalism and the Gamma distribution, which are both presented below.

2.2 Normalization and Limits

For some closure methods, the moments require normalizing. This is done either to ensure the distribution is between certain limits such as the interval of 0 to 1, or more generally, to reduce the numerical difference between moments. In either case, a normalizing length scale is required. Using the ratio of any pair of successive moments a normalization radius r_n can be defined,

$$r_n = \frac{\mu_{i+1}}{\mu_i}. \quad (4)$$

This radius can then be used to provide a sensible range in which the upper limit lies. From numerical tests, the upper limit can be assumed to lie in the range $r_n < r_u < 3.5 r_n$ (for $n = 2$) and the lower limit, r_l , set to zero.

Upon establishing a normalizing length scale, r_n , and before the closure method is called, linear normalization of the moments is performed by substitution of $x = \frac{r}{r_n}$ into Eq. (1), giving

$$\frac{\mu_i}{\mu_0 r_n^{1+i}} = \int_{r_n x}^{\infty} \phi(r_n x) x^i dx \quad (5)$$

2.3 Maximum Entropy Distribution

The probability density function is approximated as ([25])

$$\phi(r) \approx p(r) \exp \left[- \sum_{i=0}^{N-1} \lambda_i r^i \right] \quad (6)$$

where N is the number of moments available and $\lambda_0 \dots \lambda_{N-1}$ are the Lagrangian multipliers and $p(r)$ is the ‘preconditioning’ approximate distribution. Different possible forms of $p(r)$ are listed in Table 2.

Table 2: Approximate distribution functions

Type	$p(r)$
Uniform	1
Mean value	r_{10}
Exponential	$\frac{1}{r_{10}} \exp\left(-\frac{r}{r_{10}}\right)$
Rayleigh	$\frac{r}{s^2} \exp\left(-0.5\frac{r^2}{s^2}\right)$, where $s = r_{10}\sqrt{0.5\pi}$
Beck ([3])	$16 \frac{r}{r_{32}^2} \exp\left(-4\frac{r}{r_{32}}\right)$

Substituting Eq. (6) into Eq. (1) provides N equations with N unknown multipliers (Eq. (7)).

$$f_j(\underline{\lambda}) = \int_r r^j p(r) \exp\left[-\sum_{i=0}^{N-1} \lambda_i r^i\right] dr = \frac{\mu_j}{\mu_0} \quad (7)$$

In order to solve the set of equations, $f_j(\underline{\lambda})$ is approximated as a first-order Taylor series, using the general form for functions with several arguments;

$$f_j(\underline{\lambda}) = \sum_{k=0} \frac{1}{k!} \frac{d^k}{d\underline{\lambda}^k} [f_j(\underline{\lambda}^0)] \cdot (\underline{\lambda} - \underline{\lambda}^0)^k \quad (8)$$

$$\approx f_j(\underline{\lambda}^0) + \frac{d}{d\underline{\lambda}} [f_j(\underline{\lambda}^0)] \cdot (\underline{\lambda} - \underline{\lambda}^0), \quad (9)$$

where the gradient of $f_j(\underline{\lambda})$ is

$$\frac{d}{d\lambda_k} [f_j(\lambda_k)] = - \int_r r^k r^j p(r) \exp\left[-\sum_{i=0}^{N-1} \lambda_i r^i\right] dr. \quad (10)$$

Rearranging Eq. (9) leads to a system of linear equations. Before the solution to these equations can be formed, the gradients must be calculated by performing numerical integration. Both tasks can be accomplished using standard mathematical library packages. Initial multipliers, $\underline{\lambda}^0$, are typically set to zero.

2.4 A-priori Distributions

There are a number of possible distributions which could be assumed to represent the underlying probability density function, such as the Log-Normal, Gamma, Beta and the Rayleigh distributions. Here, only the Gamma distribution will be developed.

The Gamma distribution is defined as

$$\phi(r) = \frac{r^{k-1}}{\Gamma(k)\theta^k} \exp\left(-\frac{r}{\theta}\right), \quad (11)$$

where

$$\Gamma(k)\theta^k = 1 \quad (12)$$

by definition. Combining Eq. (11) and Eq. (1) gives

$$\begin{aligned} \frac{\Gamma(k)\theta^k \mu_j}{\mu_0} &= \int_0^\infty r^{k-1+j} \exp\left(-\frac{r}{\theta}\right) dr \\ &= \left[-\theta r^{k-1+j} \exp\left(-\frac{r}{\theta}\right)\right]_0^\infty + \theta(k-1+j) \int_0^\infty r^{k-2+j} \exp\left(-\frac{r}{\theta}\right) dr \\ &= \frac{\theta(k-1+j)\mu_{j-1}}{\mu_0}, \end{aligned} \quad (13)$$

which simplifies to

$$\frac{\mu_{j+1}}{\mu_j} = \theta(k+j). \quad (14)$$

From Eq. (14), the parameters can be related to three consecutive moments by

$$k = \frac{j \left(1 - \frac{\mu_{j+2}\mu_j}{\mu_{j+1}^2}\right) + 1}{\frac{\mu_{j+2}\mu_j}{\mu_{j+1}^2} - 1} \quad (15)$$

$$\theta = \frac{\mu_{j+1}}{\mu_j(k+j)}. \quad (16)$$

To ensure the denominator of the above equation remains unconditionally positive, limits are set on parameter k such that $1.5 < k < 20$. Moments of the Gamma distribution can be calculated by

$$\mu_\alpha|_{r_l}^{r_u} = \mu_0 \theta^\alpha \frac{\Gamma(k+\alpha)}{\Gamma(k)} \left[\gamma\left(k+\alpha, \frac{r_u}{\theta}\right) - \gamma\left(k+\alpha, \frac{r_l}{\theta}\right) \right], \quad (17)$$

where $\gamma(k, x)$ is the lower incomplete Gamma function.

3 Moment Averaged Properties

The manner in which intensive properties of the droplets, such as temperature and velocity, vary with droplet size may be captured in a similar way to the moments capturing the variation of the underlying distribution. By averaging such a property, $\psi(r)$, over the probability density function, moment averaged quantities, Ψ_i , are obtained by

$$\Psi_i = \frac{\int_r \phi(r) r^i \psi(r) dr}{\int_r \phi(r) r^i dr} \quad (18)$$

$$= \frac{\mu_0}{\mu_i} \int_r \phi(r) r^i \psi(r) dr \quad (19)$$

In [20] it was shown that whilst the determination of the probability density function in Eq. (1) is ill-conditioned, determination of functionals like $\psi(r)$ in Eq. (19) is well conditioned and can be reliably determined, assuming that Ψ_i and $\phi(r)$ are known.

The method employed here for approximating the droplet velocity profile (Eq. (20), [10]) assumes that for small droplets, their velocity, \vec{v}_d , increases rapidly from the surrounding gas velocity, \vec{v} , with increasing droplet radius and for large droplets, velocity increases slowly (for $0 < b < 1$).

$$\vec{v}_d(r) = \vec{v} + \vec{a}_i r^b \quad (20)$$

The coefficient, \vec{a}_i , is determined by substituting Eq. (20) into Eq. (19), giving

$$\vec{a}_i = (\vec{V}_{d,i} - \vec{v}) \frac{\mu_i}{\mu_{i+b}} \quad (21)$$

where $\vec{V}_{d,i}$ is the i^{th} moment averaged velocity. Equation (20) implies that an individual drop velocity is a function of moments, which is not true. To compensate for this inconsistency, the index i is taken to be 3, weighting the distribution on the behaviour of the volumetric moment transportation.

4 Transport Equations

The derivation of the moment and moment-averaged momentum conservation equations for the spray model begins with stating the derivative of a fluid particle (droplet) property, ϕ , per unit volume with respect to time which is travelling at velocity \vec{v}_d and has a density ρ_d [22]:

$$\rho_d \frac{d(\phi)}{dt} = \rho_d \left(\frac{\partial}{\partial t}(\phi) + \vec{v}_d \cdot \text{grad}\phi \right) \quad (22)$$

This represents the change of the droplet property as it is being followed along its pathline. However, in the context of the spray model, the quantities being transported will be integral quantities, i.e. the moments are integrals of the droplet size distribution within a given region and are used to represent averaged quantities, such as the local SMR, which indicates that Eq. (22) would be better represented in an Eulerian manner. The relationship between Eq. (22) and the equivalent Eulerian description is

$$\rho_d \left(\frac{\partial}{\partial t}(\phi) + \vec{v}_d \cdot \text{grad}\phi \right) = \frac{\partial}{\partial t}(\rho_d \phi) + \text{div}(\rho_d \vec{v}_d \phi) - \phi \left(\frac{\partial}{\partial t}(\rho_d) + \text{div}(\rho_d \vec{v}_d) \right) \quad (23)$$

Casting the above equation into the generalised form for a transported property and applying Gauss' theorem, the template transport equation becomes (with the inclusion of source terms)

$$\frac{\partial}{\partial t} \int_{\Omega} \rho_d \phi \, d\Omega + \int_S \rho_d [\vec{v}_d \cdot \vec{n}] \phi \, dS - \phi \left(\frac{\partial}{\partial t} \int_{\Omega} \rho_d \, d\Omega + \int_S \rho_d [\vec{v}_d \cdot \vec{n}] \, dS \right) = \int_{\Omega} q_{\phi} \, d\Omega \quad (24)$$

where q_{ϕ} represents any additional contributions to the rate of change of the transported property.

In order to arrive at the governing equations of the spray model, the equations for a moment about the origin (Eq. (1)) and a moment-averaged property (Eq. (19)) are introduced to Eq. (24), forming two conservation equations: when ϕ represents a moment of the PDF and when ϕ represents a moment-averaged velocity of the PDF.

4.1 Continuity

Replacing \vec{v}_d with the moment-averaged velocity and ϕ with the transported moment, μ_i in Eq. (24), the moment continuity equation becomes (N.B. $\phi(r)$ is the PDF)

$$\begin{aligned} \frac{\partial}{\partial t} \int_{\Omega} \left\{ \mu_0 \int_r \phi(r) r^i \, dr \right\} \, d\Omega + \int_S \left[\left\{ \frac{\mu_0}{\mu_i} \int_r \phi(r) r^i \vec{v}_d(r) \, dr \right\} \cdot \vec{n} \right] \left\{ \mu_0 \int_r \phi(r) r^i \, dr \right\} \, dS \\ = \int_{\Omega} \left\{ \mu_0 \int_r \phi(r) q_i(r) \, dr \right\} \, d\Omega \end{aligned} \quad (25)$$

Since heat transfer is not considered, Eq. (24) is divided through by ρ_d (see [23] for modifications when considering heat transfer). The third term in Eq. (24) is equal to zero by virtue of moment conservation.

The resulting transport equation, upon integration over all droplets, represents the conservation of moments (Eq. (26)) and is analogous to the mass conservation (per unit volume) of the continuum phase. The moments represent quantity (per unit volume) and those moments are convected by their moment-averaged velocity.

$$\frac{\partial}{\partial t} \int_{\Omega} \mu_i d\Omega + \int_S [\vec{V}_{d,i} \cdot \vec{n}] \mu_i dS = \int_{\Omega} q_{\mu_i} d\Omega \quad (26)$$

4.2 Momentum

The moment-averaged momentum transport equation (Eq. 27) has its respective moment as the coefficient since the moment represents quantity per unit volume. The derivation of this follows the same method as above.

$$\begin{aligned} \frac{\partial}{\partial t} \int_{\Omega} \mu_i \vec{V}_{d,i} d\Omega + \int_S \mu_i [\vec{V}_{d,i} \cdot \vec{n}] \vec{V}_{d,i} dS \\ - \vec{V}_{d,i} \left(\frac{\partial}{\partial t} \int_{\Omega} \mu_i d\Omega + \int_S [\vec{V}_{d,i} \cdot \vec{n}] \mu_i dS \right) = \int_{\Omega} q_{\vec{V}_{d,i}} d\Omega \end{aligned} \quad (27)$$

Here it is noted that although the above transport equations are written for a particular moment, i , one moment cannot be considered separately from the set of transported moments corresponding to the same underlying distribution. Within a given region, all related transported moments must co-exist, otherwise none of the moments must exist.

4.3 Liquid Film

Since there is a possibility of droplets sticking to the wall upon impaction, the resulting formation of a liquid film must be accounted for. This film does not need to be transported (the convection term may be omitted) so long as the near wall control-volumes are sufficiently large to prevent non-physical liquid volume fractions. The liquid film volume fraction equation is then defined as

$$\frac{\partial}{\partial t} \int_{\Omega} \theta d\Omega + \int_S [\vec{v}_{\theta} \cdot \vec{n}] \theta dS = \int_{\Omega} q_{\theta} d\Omega \quad (28)$$

In the methodology presented, the velocity of the film, \vec{v}_{θ} , will be assumed to be zero, effectively grouping together the adhering and spreading droplets resulting from impaction of the spray. Details on extending the liquid film modelling can be found in [19].

5 Physical Processes

5.1 Inter-phase Drag

The rate of change of momentum of a droplet equals the sum of the forces acting on the droplet

$$m_d \frac{D\vec{v}_d}{Dt} = \sum \vec{F}_d \quad (29)$$

The drag force, \vec{F}_{dr} , is the dominant force acting on a droplet and is given in [6]

$$\vec{F}_{dr} = \frac{1}{2} C_d \rho A_d \parallel \vec{v} - \vec{v}_d \parallel (\vec{v} - \vec{v}_d). \quad (30)$$

where the drag coefficient is defined as

$$C_d = \begin{cases} 24Re_d^{-1} + 3.48Re_d^{-0.313} & \text{if } 0 < Re_d \leq 1000 \\ 0.424 & \text{if } Re_d > 1000, \end{cases} \quad (31)$$

and the Reynolds number as

$$Re_d = \frac{2\rho \parallel \vec{v} - \vec{v}_d \parallel r}{\mu} \quad (32)$$

The form of the drag coefficient is based on empirical data of [14]. The source term contribution due to inter-phase drag is defined as

$$\vec{q}_{\vec{v}_d, i} = \mu_0 \int_r \frac{d\vec{v}_d}{dt} \phi(r) r^i dr \quad (33)$$

where the acceleration of an individual droplet is

$$\frac{d\vec{v}_d}{dt} = \frac{3}{8} \frac{\rho}{\rho_d} \frac{C_d}{r} \parallel \vec{v} - \vec{v}_d(r) \parallel (\vec{v} - \vec{v}_d(r)) \quad (34)$$

In order to equate the rate of change of the moment-averaged momentum with Eq. (30), a number of steps are required. First, \vec{v}_d needs to be replaced by the moment dependent relation, $\vec{v}_d(r)$ and secondly, the instantaneous continuum velocity, \vec{v} , requires approximating.

The velocity, \vec{v} , is decomposed into its mean and fluctuating component, whereby the mean velocity is that solved by the continuum momentum equation and the fluctuating velocity is approximated using the turbulent kinetic energy, k , provided by the turbulence model, as

$$\vec{v}' = (\vec{\gamma} - 0.5) \sqrt{\frac{2}{3}k} \quad (35)$$

where $\vec{\gamma}$ is randomly generated in the interval $\vec{0} - \vec{1}$.

The drag term can either be evaluated analytically, performing a summation of three integrals (assuming the functional form of the velocity distribution is of a simple form), or numerically by discretizing the PDF and the droplet velocity profile. For analytical integration the conditions relating to the drag coefficient in Eq. (31) are rearranged to provide critical radii, r_a and r_b respectively. The drag term is then made up of three parts: the integral of Eq. (33) between 0 and r_a , r_a and r_b and lastly between r_b and ∞ .

5.2 Droplet Break-up

Three break-up models are presented. The first model of [17] encompasses all the known break-up phenomena. The second model of [8] is applicable for diesel spray cases, whereby no categorizations are made regarding the droplet break-up methods. Lastly, the model of [18] considers secondary break-up only; that of bag and stripping break-up.

With all the models, the manner in which they contribute to the source terms of the moments equations is the same, only the number of droplets produced, N_b , and the time-scale for this process, τ_b , differs between the models. The equations below are presented here to show how

any given break-up model contributes to any transported moment (and that no contribution is made for μ_3).

The source term contribution to the moment transport equations due to break-up is of the form

$$q_{\mu_i} = \mu_0 \int_r \frac{\delta r^i}{\delta t} \phi(r) dr \quad (36)$$

where

$$\frac{\delta r^i}{\delta t} = \frac{(N_b^{\frac{3-i}{3}} - 1) r^i}{\tau_b} \quad (37)$$

The number of droplets produced from the break-up of a single droplet is determined by considering droplet volume conservation, giving

$$N_b = \left(\frac{r}{r_{st}} \right)^3 \quad (38)$$

where r_{st} is the stable droplet radius.

None of the resultant terms of the break-up models are presented in integral form, although the first model can be integrated analytically [4]. The remaining models must be either integrated numerically or approximated to enable analytical integration. In this work the former method is implemented.

5.2.1 Pilch and Erdman Model

Break-up occurs if

$$We = \frac{2\rho \|\vec{v} - \vec{v}_d\|^2 r}{\sigma_d} > We_{crit} \quad (39)$$

where the critical weber number $We_{crit} = 12(1 + 1.077 Oh^{1.6})$. Break-up phenomena are distinguished by their dimensionless break-up time, defined as

$$T = \begin{cases} 6(We - 12)^{-\frac{1}{4}} & \text{if } 12 < We \leq 18 \\ 2.45(We - 12)^{\frac{1}{4}} & \text{if } 18 < We \leq 45 \\ 14.1(We - 12)^{-\frac{1}{4}} & \text{if } 45 < We \leq 350 \\ 0.766(We - 12)^{\frac{1}{4}} & \text{if } 350 < We \leq 2670 \\ 5.5 & \text{if } We > 2670 \end{cases} \quad (40)$$

The break-up time-scale then is calculated, using T , giving

$$\tau_b = 2T \frac{r}{\|\vec{v} - \vec{v}_d\|} \sqrt{\frac{\rho_d}{\rho}} \quad (41)$$

The stable droplet radius is found from

$$r_{st} = \frac{We_{crit} \sigma_d}{\rho \|\vec{v} - \vec{v}_d\| (1 - V_d)^2} \quad (42)$$

where

$$V_d = (0.375T + 0.2274T^2) \sqrt{\frac{\rho}{\rho_d}} \quad (43)$$

5.2.2 Reitz and Diwakar Model

This model considers two kinds of break-up; bag break-up which is caused by a non-uniform pressure field around the droplet and stripping break-up which is caused by the droplet being sheared. For both cases the condition for the onset of break-up and the stable radius is determined by the same inequality.

Bag Break-up Instability is determined by the Weber number

$$We = \frac{\rho \|\vec{v} - \vec{v}_d\|^2 r}{\sigma_d} \geq C_{b,1}, \quad (44)$$

where $C_{b,1}$ is an empirical coefficient in the range 3.6 to 8.4. The associated time scale is

$$\tau_b = C_{b,2} r^{\frac{3}{2}} \left(\frac{\rho_d}{\sigma_d} \right)^{\frac{1}{2}} \quad (45)$$

where $C_{b,2} \approx 2.22$.

Stripping Break-up Instability is determined by

$$\frac{We}{\sqrt{Re_d}} = \|\vec{v} - \vec{v}_d\|^{\frac{3}{2}} r^{\frac{1}{2}} \left(\frac{\mu\rho}{2} \right)^{\frac{1}{2}} \geq C_{s,1} \quad (46)$$

where $C_{s,1} = 0.5$. The associated time scale is

$$\tau_b = \frac{C_{s,2} r}{\|\vec{v} - \vec{v}_d\|} \left(\frac{\rho_d}{\rho} \right)^{\frac{1}{2}} \quad (47)$$

where $C_{b,2}$ is an empirical coefficient in the range 2 to 20.

5.2.3 Hsiang and Faeth Model

For diesel sprays the following model encompasses all break-up regimes. Break-up takes place if the $We > 6$ and the model is valid for Weber numbers less than 1000. The stable diameter is defined as

$$r_{st} = 6.2 r^{\frac{1}{2}} \left(\frac{\rho}{\rho_d} \right)^{\frac{1}{4}} \sqrt{\frac{\mu_d}{\rho_d \|\vec{v} - \vec{v}_d\|}} \quad (48)$$

and the corresponding time-scale is

$$\tau_b = \frac{5}{1 - Oh/7} \frac{r_d}{\|\vec{v} - \vec{v}_d\|} \sqrt{\frac{\rho_d}{\rho}} \quad (49)$$

5.3 Droplet Collisions

The collision model is based on the work of [15] and applied here only to its effects on the moments. This simplifies the model by only considering coalescence. Separation and bounce have no effect on the droplet size distribution. The form of the source term contribution is similar to that of the break-up. Here, the number of droplets undergoing coalescence is determined by empirical and statistical methods in addition to critical radii conditions.

The coalescence of N_d donor droplets of radius r_d with a collector droplet of radius r_c , results in

$$\frac{\delta r^i}{\delta t} = \frac{1}{\delta t} \sum_{r_d}^{r_c} \left[(r_c^3 + N_d r^3)^{\frac{i}{3}} - r_c^i - N_d r^i \right] \quad (50)$$

The number of donor droplets undergoing coalescence is determined by the following method: The probability of a collector droplet undergoing N collisions with droplets of size r_d in the time interval δt is assumed to follow a Poisson distribution

$$P_N = \frac{\bar{n}^N}{N!} e^{-\bar{n}} \quad (51)$$

where the mean number of collisions is defined as

$$\bar{n} = \pi(r_d + r_c)^2 \parallel \vec{v}_c - \vec{v}_d \parallel \delta t \frac{N_d}{\delta \Omega} \quad (52)$$

Whilst there may be the possibility of P_N collisions based on above two equations, the term $\parallel \vec{v}_c - \vec{v}_d \parallel$ does not take into account whether the droplets are heading towards each other or not. The information required to determine this is not available in the moments methodology so a random number between 0 and 1 is used. If the random number is greater than 0.5, the droplets will collide.

Since not all collisions result in coalescence, the probability that coalescence takes place is

$$P_{coal} = \min \left[2.4 \frac{f(\gamma)}{We_L}, 1 \right] \quad (53)$$

where $\gamma = r_c/r_d$ and

$$f(\gamma) = 2.7\gamma - 2.4\gamma^2 + \gamma^3 \quad (54)$$

and

$$We_L = \frac{\rho_d \parallel \vec{v}_c - \vec{v}_d \parallel^2 r}{\sigma_d} \quad (55)$$

By generating two random numbers, $N_{r,1}$ and $N_{r,2}$, in the interval $(0 - 1)$ the actual occurrence of a collision taking place is if $N_{r,1} > P_{N=0}$. If collisions take place then coalescence is the result of that collision if $P_{coal} < N_{r,2}$ and the number of donor droplets involved is found from the Poisson distribution, such that

$$\sum_{i=0}^{N-1} P_i < N_{r,1} < \sum_{i=0}^N P_i \quad (56)$$

6 Injection Conditions

6.1 Injector

The approach used in this methodology is to resolve the actual size of the nozzle orifice (Fig. 1(a)), rather than projecting a larger equivalent orifice in front of the injector [3]. The actual injector is represented computationally by the overall shape of the injector tip (Fig. 1(b)). The modelled nozzle orifice is protruded slightly in order to clarify its size.

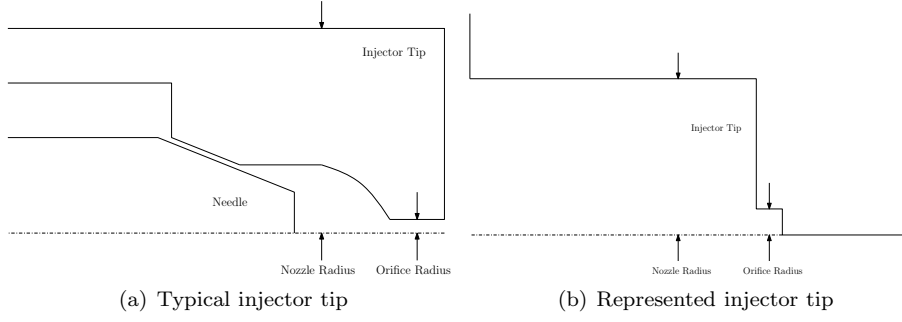


Figure 1: Schematics of the spray injector

6.2 Injected Moments

Moments of the injected droplet size distribution are based on the Gamma distribution [26]. Specifying three parameters: the liquid volume fraction, Θ , Sauter mean radius, r_{32} and the skewness parameter, k , the first two parameters μ_3 and μ_2 are found by

$$\mu_3 = \frac{\Theta}{\frac{4}{3}\pi} \quad (57)$$

$$\mu_2 = \frac{\mu_3}{r_{32}} \quad (58)$$

and all other moments are determined recursively using the relation

$$\frac{\mu_{i+1}}{\mu_i} = r_{32} \frac{k+i}{k+2} \quad (59)$$

The three parameters are related to the nozzle orifice radius, the injector operating conditions and how the nozzle orifice is modelled. Since the nozzle orifice is resolved, the exiting liquid volume fraction will be high ($0.9 - 1$). Such a high volume fraction is inconsistent with the assumption that the liquid is in the form of spherical droplets, though for the sake of resolving the injector and maintaining a simple injection model, this inconsistency is not rectified in this work.

The exiting bulk liquid is assumed to have been broken up into droplets, so the Sauter mean radius is approximated to be in the range $0.05r_{orif} - 0.15r_{orif}$. Finally, because only break-up of bulk liquid has taken place, the relative number of smaller droplets (than the mean) will be low, implying that the distribution will only have a weak positive skew, leading to a range of $3 - 7$ for parameter k .

6.3 Injection Velocity

From the ambient pressure and the operating pressure of the injector, the average speed of the exiting liquid and entrained gas can be approximated by

$$U = C_d \sqrt{\frac{2(P_{inj} - P_{amb})}{\rho_d}} \quad (60)$$

where the discharge coefficient, C_d , is approximately 0.7. The spray half-cone angle is then used to obtain the orifice outermost velocity. The variation of velocity towards the axis is controlled by an appropriate radial profile.

7 Impaction Conditions

Wall boundary conditions are based on the spray impingement model of [2], where the condition of the wall and the state of the impinging spray determine the outcomes. If the wall is dry the velocity and moments of the splashing droplets are determined. If the wall is wet, rebounding conditions in addition to splashing conditions are defined. An alternative model is described by [7] though is not considered here.

At the wall face (Fig. 2), the splashing and rebounding conditions are determined from the near-wall control volume injected spray state. The impacting spray boundary conditions at the wall are defined as being permeable, i.e. the spray passes through the wall. This prevents a build-up of moments in the near-wall control volume. To represent the build-up of liquid which actually would occur, the sum of the μ_3 fluxes at the wall (multiplied by $\frac{4}{3}\pi$) becomes the source term for the liquid film equation.

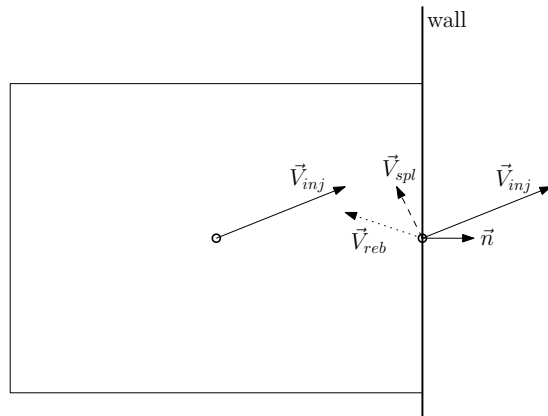


Figure 2: Division of the spray into injected, splashing and rebounding sprays

7.1 Critical Radii

In order to determine which droplets undergo the different processes, critical radii are obtained from the following correlations. Splashing and rebounding moments are calculated from integrating the near-wall PDF of the incoming spray between the limits prescribed by the critical radii. Moment-averaged splashing and rebounding velocities are calculated in a similar manner.

7.1.1 Dry Walls

Splashing takes place when

$$We_d La^{0.18} > C_{1,d} \quad (61)$$

where La is the Laplace number, defined as

$$La = \frac{2\rho_d \sigma_d r}{\mu_d} \quad (62)$$

$C_{1,d}$ is related to the wall roughness r_s by

$$C_{1,d} \approx 2588 r_s^{-0.254} \quad (63)$$

for wall roughness $0.05 \leq r_s \leq 12 \mu m$.

7.1.2 Wet Walls

Rebound takes place when

$$We_d < 5 \quad (64)$$

and splashing when

$$We_d La^{0.18} > 1320 \quad (65)$$

Droplets outside these ranges for both wet and dry walls are assumed to stick. From these conditions, critical radii are determined and then used to integrate over the near-wall droplet distribution, obtaining the appropriate boundary condition moments for the splashing and rebounding spray. A droplet undergoing splashing is assumed to break up into N_{spl} droplets (taken as equal to 2 by [11]), resulting in

$$\mu_i = N_{spl}^{\frac{3-i}{2}} \mu_{i,spl}. \quad (66)$$

7.1.3 Transition

In practice, the wall becomes wet over the duration of the spray impacting on the wall. This transition should be considered rather than assuming that either the wall is wet or dry from the outset. To perform this transition, the method proposed here compares the volume fraction of the liquid film on the wall with a critical film volume fraction, θ_{wet} , to determine whether the wall is wet. If the volume fraction is less than the critical value and non-zero, the coefficient $C_{1,d}$ is modified by the function

$$C_{1,d} = \frac{1320 - C_{1,d}}{\theta_{wet}} \theta + C_{1,d} \quad (67)$$

and the wall is assumed to be dry. The critical film volume fraction is taken as 0.01.

7.2 Resultant Velocities

Corresponding droplet velocities are calculated from the volume-averaged incoming velocity and the wall normal vector.

$$\vec{v}_{in} = \vec{v}_d(r) \quad (68)$$

$$\vec{v}_n = (\vec{v}_{in} \cdot \vec{n}) \vec{n} \quad (69)$$

$$\vec{v}_t = \vec{v}_{in} - \vec{v}_n \quad (70)$$

$$\vec{v}_{out} = -C_n \vec{v}_n + C_t \vec{v}_t \quad (71)$$

For rebounding droplets, the process is assumed to be inelastic, resulting in the coefficients taking

$$C_n = 0.993 - 1.76\theta + 1.56\theta^2 - 0.49\theta^3 \quad (72)$$

$$C_t = 0.714 \quad (73)$$

where θ is the incidence angle. Splashing droplets take identical coefficients of 0.25 [11].

Upon integrating between the limits for the splashing and rebounding conditions, two set of moments and moment-averaged velocities will be obtained (for splashing spray and the rebounding spray). The likelihood is that within either set, the moment-averaged velocities will be dissimilar (assuming a non-uniform droplet velocity profile), potentially becoming a source of divergence for the model. To overcome this, the fourth moment-averaged velocities ($\vec{V}_{d,3,spl}$ and $\vec{V}_{d,3,reb}$) are used for all moments within their respective sets.

8 Spray Model Parameters

There are a number of parameters and submodels to choose from in order to define the complete spray model. This section is presented in order to show how the different parameters and submodels effect the overall spray and to come to conclusions about which parameters and submodels are most suitable.

The suitability of the choice of parameters and submodels is defined by meeting two conditions. First, that with a given configuration, the complete spray model remains stable throughout the entire simulation, and secondly, the Sauter mean radius (SMR) is physically sensible in all regions of the spray.

The range of parameters and submodels are listed in Table 3, where the initial reference parameters (and submodels) are shown in bold font and ideal parameters are marked by an asterisk. After a parametric case is performed, reference parameters referring to that case may be modified, whereby the modified parameters are used for subsequent parametric cases.

The computational grid, fluid properties and other configuration details of the test cases are exactly the same as those found in Sect. 9 detailing the wall impaction case.

Table 3: Parameters and submodels

Parameter/submodel	Options
Moments conv. bl. (HRIC)	0 , 0.3, 0.6, 0.9
Velocity conv. bl. (TVD: Min-mod)	0 , 0.3, 0.6, 0.9
Break-up model	RD, PE* , HF
Velocity exponent, b	0.2, 0.4 , 0.6
Collision model	Off , On*
SMR at injector, $r_{32,inj}$ (μm)	15, 25 , 35
Skewness of inj. PDF, k_{inj}	3, 7
Temporal scheme	EI2, EI3*
Time step, Δt (μs)	1, 2 , 3*
Moments, P_μ [—]	[1 2 3], [2 3 4], [3 4 5], [0 1 2 3], [0 1 2 3 4]*

The overall shape of the spray is expected to be strongly effected by the accuracy at which the spray properties are convected and so the convection schemes are assessed first. Once the choice of blending for the moments and their momentums are decided, the break-up models are compared. As noted in the methodology, only the break-up model of [17] (PE) covers all break-up regimes for any type of spray so is expected to be the model adopted. However, all three models are compared and are considered as suitable candidates. Velocity exponent is then varied to find out what degree of influence this has on the spray and then the collisions model is introduced.

Parameters of the injected distribution are not expected to have a strong effect on the overall spray. If the SMR is over-predicted, the break-up model should suitably reduce this and the collisions model is expected to compensate to some degree for an excessively positive-skew distribution. Here, this hypothesis is tested.

Comparison between the Euler implicit temporal discretization schemes is performed only to show whether adopting a three time levels method (EI3) makes any noticeable difference to the spray over the two time levels method (EI2). Very little difference, if any, is expected, since geometrical errors are expected to considerably out-weight temporal discretization errors, especially since the grid topology is non-orthogonal.

Convergence with a time step as large as $3\mu s$ is not expected, though is tested anyway. For the majority of cases found in [3], the time step was set as $1\mu s$. With improved temporal discretization (EI3), the possibility of using a larger time step is sought.

Finally, once all the major components of the spray model are set, the choice of transported moments is assessed. For the first three cases, the PDF will be reconstructed using the Gamma distribution, and for the last two cases, the Maximum Entropy method will be used as the primary choice and as the secondary choice the Gamma distribution will be used, based on the three highest order moments available ([1 2 3] and [2 3 4] respectively).

N.B. All graphed SMR data presented is taken from the chordline of the spray as shown in Fig. 3.

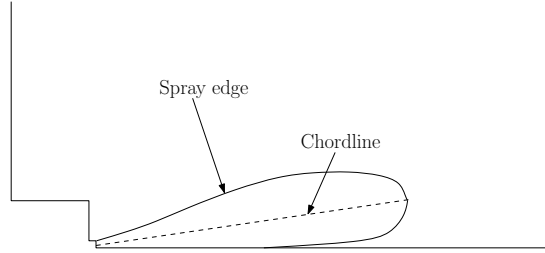


Figure 3: Chordline of the injected spray

8.1 Number of Segments

Before beginning the parametric cases, the number of segments required for the discretization of the PDF and droplet velocity profile is determined by plotting the cumulative inter-phase drag source term (since contributions to the source term are made over the entire droplet size range, unlike break-up and collision terms). Figure 8.1 shows that whilst the cumulative term for the range of segmentations is almost identical (the source term can be calculated accurately with as few as 10 segmentations), the intermediate contributions converge with 40 segmentations.

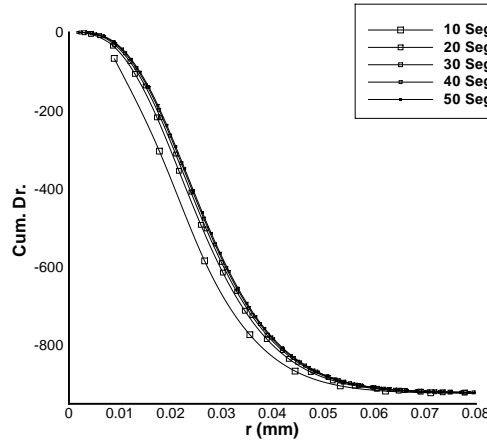


Figure 4: Convergence obtained for 40 segmentations

With 40 segmentations, the computational time required to solve the hydrodynamics was found to be disproportionate to the time required to solve the spray transport equations. As a result, the number of segmentations performed on the underlying distributions is reduced to 30.

8.2 Convection Schemes

The testing of the convection schemes breaks down into two sections; first the spray alone is transported without spray hydrodynamics activated (inter-phase drag and break-up) as a means of testing the boundedness of the transported moments for the various configurations. Once a suitable configuration is found, the hydrodynamics terms are activated and the spray model is tested with the optimal choice of convection schemes blending.

To determine whether the spray is being modelled in a bounded manner, the SMR is calculated. If the SMR deviates from the inlet SMR then the solution is not bounded. Both the min-mod total variation diminishing (TVD) scheme and the high resolution interface capturing (HRIC) scheme [13] are blended with the implicitly implemented upwind differencing scheme (UDS). The degree to which the high order scheme is blended with the UDS scheme is listed in Table 3.

First, the calculated spray shape is shown in Fig. 5 using UDS for both the moments and their momentum. This shows excessive false diffusion, as shown by the presence of the spray above the theoretical outer edge (determined from the injection angle) shown by the grey line cutting through the spray. SMR is constant throughout the spray.

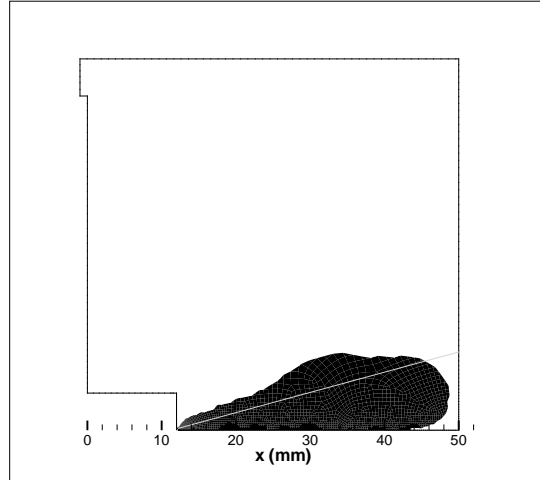


Figure 5: Spray shape with pure UDS

8.2.1 Deferred Correction and Blending

The method for implementing a higher order interpolation scheme to compute cell face fluxes (F_k) is to use the lower order scheme (UDS) to discretize the term to form the matrix entries and include the difference between the higher order scheme (HRIC or TVD) and the lower order scheme based on current values of the transported field in the right-hand side (the source term), as in

$$F_k = F_k^L + \gamma(F_k^H - F_k^L)^{curr} \quad (74)$$

Normally, a value of γ is set for each transport equation, typically in the range (0.5 - 1).

When solving the moment-averaged momentum equations using a high order convection scheme, it was found that augmentations to the source term by Eq. (74) must be zeroed where the spray does not exist, as shown in Fig. 6. This step is essential for the spray to be transported using high-order convection schemes.

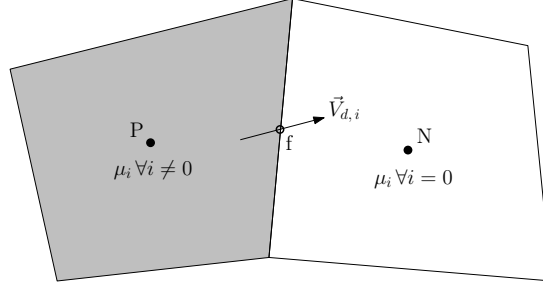


Figure 6: $(F_k^H - F_k^L)^{curr}$ is set to zero in volume N since the spray is not present there.

8.2.2 Moments

The effect of increasing the weighting of the HRIC on the moments is tested first (with UDS for momentum). From Fig. 7 the trend shown is that increasing the weighting towards the HRIC scheme, the spray shape becomes more sharply defined, reducing false diffusion. The boundedness condition is perfectly satisfied, as shown in Fig. 9.

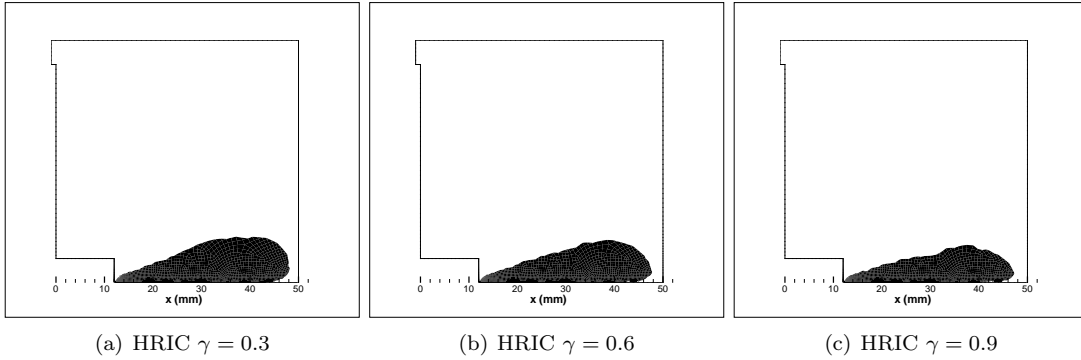


Figure 7: Variation of spray shape due to HRIC interpolation

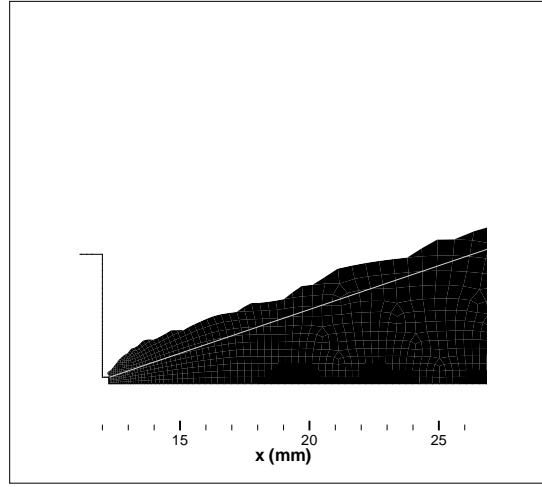


Figure 8: Radial diffusion along outer spray edge (HRIC $\gamma = 0.6$)

In addition to sharpening the spray shape, the penetration is reduced slightly with increasing γ , though there remains near-uniform radial diffusion along the outer edge of the spray which is present regardless of the value of the blending constant (Fig. 8). This radial diffusion may be related to the manner in which interpolation is performed between radially adjacent CV convection coefficients (particularly μ_i in the flux term $\mu_i[\vec{V}_{d,i} \cdot \vec{n}]$ from Eq. (27)). Further from the axis, volumetric values have greater influence so using linear interpolation (which does not account for volumetric change) will tend to exaggerate the influence of the CV values closer to the centreline, causing excess radial spread, as seen in Fig. 8.

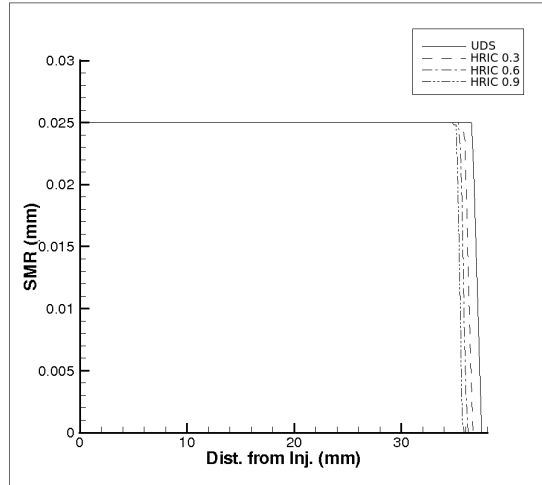


Figure 9: Boundedness of spray using HRIC

8.2.3 Momentum

The TVD scheme is the most appropriate higher order interpolation scheme to use for the momentum equations, since central differencing tends to cause unbounded solutions and HRIC

is designed for resolving scalars (particularly concentrations). With the TVD scheme, a number of interpolation functions are available, but here only the Min-mod interpolation is tested (with UDS for the moments).

Sharpness of the spray shape is not effected by the increased weighting of the TVD scheme on the momentum (Fig. 10), but the penetration is reduced to a much greater degree with the increased influence of the TVD scheme (Fig. 11) than compared with the previous case. Again the SMR is perfectly bounded.

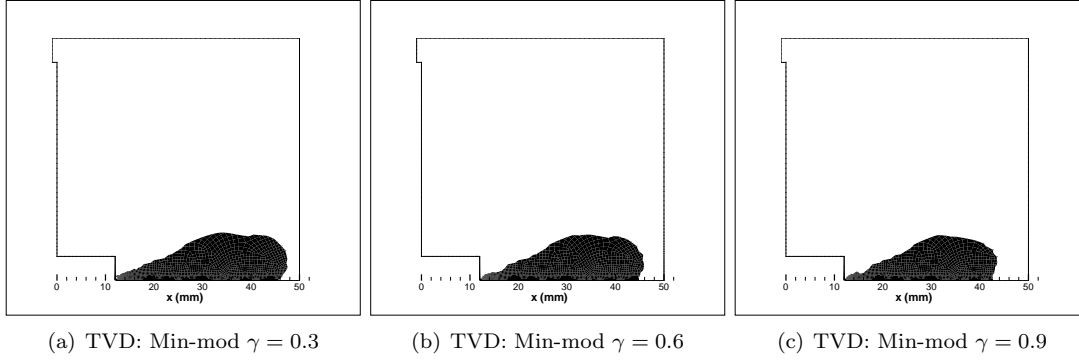


Figure 10: Variation of spray shape due to TVD interpolation

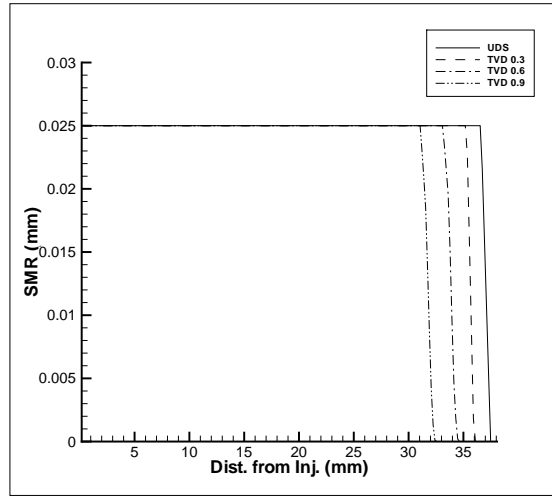


Figure 11: Boundedness of spray using TVD

8.2.4 Moments and Momentum

Combining the blending of both the moments and their momentum, three further cases were performed (HRIC/TVD $\gamma = 0.3$, HRIC/TVD $\gamma = 0.6$ and HRIC/TVD $\gamma = 0.9$). However, only the first case ran successfully and is documented below, in Fig. 12. There is no obvious reason why the second and third case failed to run properly since independently, both schemes have been shown to work, though it may be due to the difficulty in converging stiffer sets of the

coupled moment and momentum equations. At 30% blending, very little difference is found in the sharpening of the spray or its penetration compared to the pure UDS case.

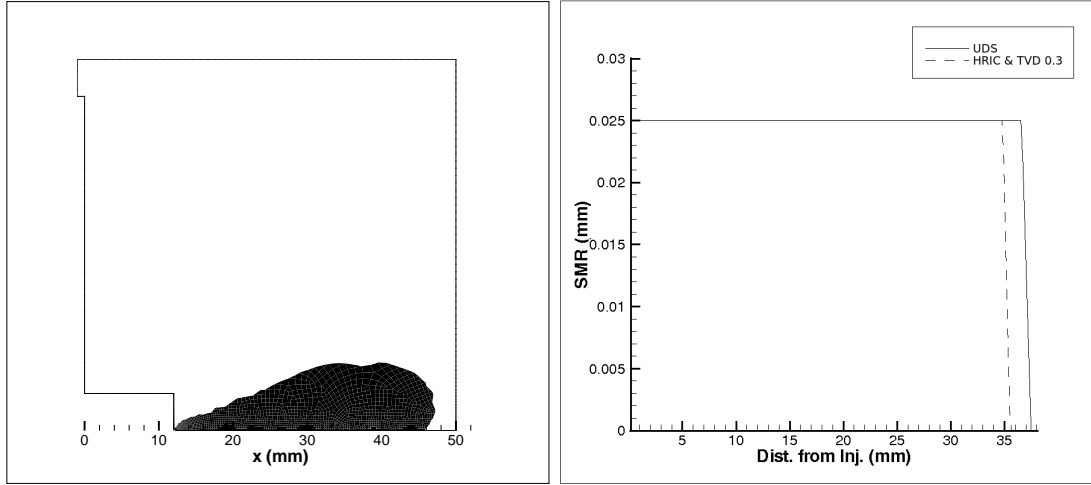


Figure 12: HRIC $\gamma = 0.3$ and TVD: Min-mod $\gamma = 0.3$

8.2.5 Optimal Blending

HRIC blending for the moments resulted in the greatest improvement in spray shape by reducing false diffusion, whereas using TVD for momentum, only the penetration was reduced. Combining the HRIC and TVD for the moments and momentum respectively caused the algorithm to become unstable for high degrees of blending.

For HRIC $\gamma = 0.9$, false diffusion is minimized, maintaining a bounded solution so the reference blending parameters are revised to HRIC $\gamma = 0.9$, TVD $\gamma = 0$. With this condition implemented and the hydrodynamics activated, the spray model was run, though as shown in Fig. 13, the SMR towards the spray tip was found to be unphysically large. Reducing the blending down to 0.6 presented a much more realistic droplet size variation.

The modification of the convection blending was not expected to have such a strong influence on the resulting SMR but only on the spray shape since its direct effect is only to cause higher concentrations in the spray by resolving its true edge more accurately. Figure 13 clearly shows, however, that the degree of blending has significant indirect influence, apparently presenting a choice between compromising on resolution of spray shape or on accuracy of the properties of the spray.

To simplify the problem, the reference break-up model (PE) was turned off and the HRIC $\gamma = 0.6$ and HRIC $\gamma = 0.9$ spray simulations were run again, leaving only the inter-phase drag model active. Figure 13 shows that without the break-up model on, the spray SMR for both cases are very similar, showing that the HRIC scheme is only influencing the spray shape, as expected, indicating that activation of the break-up model and variation of the HRIC blending somehow promotes significant changes in the spray.

The prediction of the SMR becomes worse for larger values of γ when the break-up model is active. Both the break-up source term and the HRIC scheme augment the right-hand side of the moments equations. When the break-up model is off, the moments equations are much less stiff than when break-up is on, making the equations much easier to converge, thus consistent behaviour is found (with regards to the SMR) for various values of γ .

The normal way to treat stiff equations is to under-relax the solution scheme. However, the moments and momentum equations are already solved with relatively low under-relaxation factors (0.7 for all spray equations are used, whereas in [3] no under-relaxation was performed). This apparently leaves no clear alternative than to make a compromise between spray shape accuracy and the accuracy of the SMR, thus the reference blending parameters are set to HRIC $\gamma = 0.6$, TVD $\gamma = 0$. To attempt to resolve the problem, the only clear way forward would be to revise the entire iterative solution scheme for solving the spray related transport equations, by introducing a robust predictor-corrector algorithm. This task however, is beyond the scope of the work.

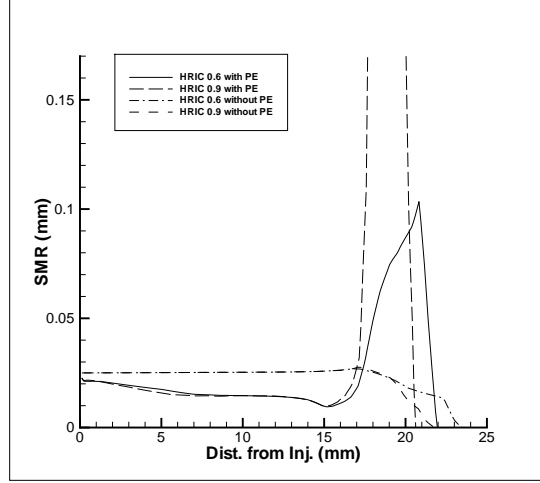


Figure 13: Effect on the SMR by HRIC and break-up

8.3 Break-up Models

Droplet break-up is shown to have a significant effect upon the spray, as shown in Fig. 14(a) - 14(b). From the comparison of the effects on the SMR by the models, two are found to be unsuitable; the models of [8] (HF) and [18] (RD). These models excessively break up droplets, resulting in a large increase in the lower moments (momentarily reducing the SMR) which causes a rapid increase in drag for their corresponding velocities (particularly the lower moment-averaged ones), leading to very large SMR at the leading edge of the spray. Only the model of [17] (PE) performs reasonably well, producing large SMR at the front end, but not to excess (Fig. 14(a)). This break-up model is now set as the revised break-up option.

The reason why two of the models appear to perform poorly is not because of the models themselves but rather that those two models are only suitable for secondary break-up processes, where primary break-up is assumed to already have taken place. The spray model is not implemented with such a condition assumed. The model of [17] compensates for this since it deals with the break-up of both primary and secondary droplets and is set as the revised parameter for this case.

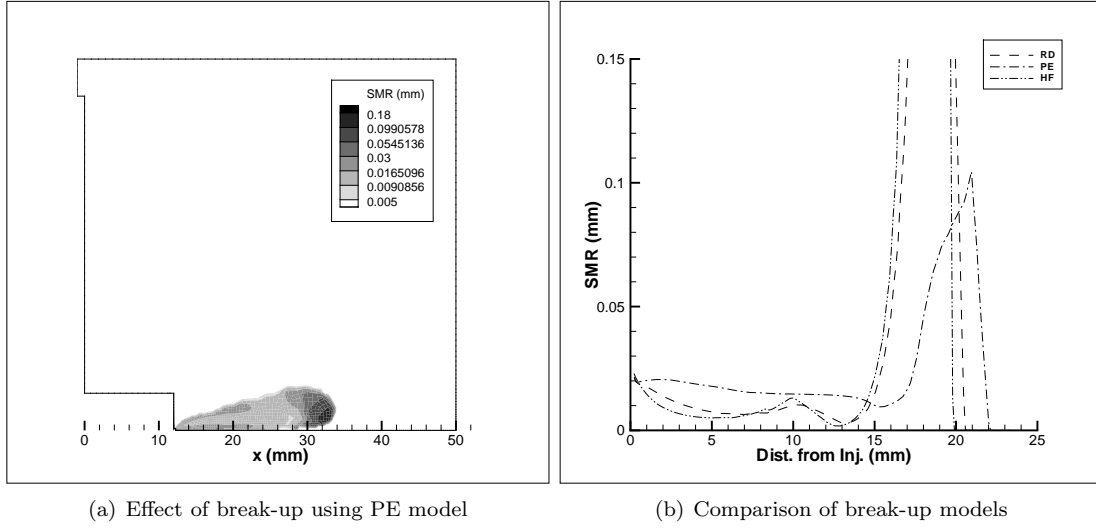


Figure 14: Effect of break-up models

8.4 Velocity Exponent

Data from three points within the spray are taken: the first is close to the injector (Point 1), the second is in the middle of the spray body (Point 2) and the last is close to the inside edge of the spray (Point 3). The extracted point data (the moments, continuum velocity and moment-averaged velocities) is shown in Table 4, with the corresponding PDFs at each point shown in Fig. 8.4.

Table 4: Extracted data from the spray

Point	μ_0 (mm^{-3})	μ_1 (mm^{-2})	μ_2 (mm^{-1})	μ_3
1	18467.9	169.204	2.03169	0.0294586
2	6201.11	48.2283	0.482322	0.00561636
3	684.43	0.894604	0.00125258	2.70287E-05

Point	v (m/s)	$V_{d,0}$	$V_{d,1}$	$V_{d,2}$	$V_{d,3}$
1	37.4231	101.471	102.005	102.318	102.437
2	11.1468	74.447	68.5326	65.2815	67.5938
3	1.2158	66.7343	57.5367	50.7085	58.2257

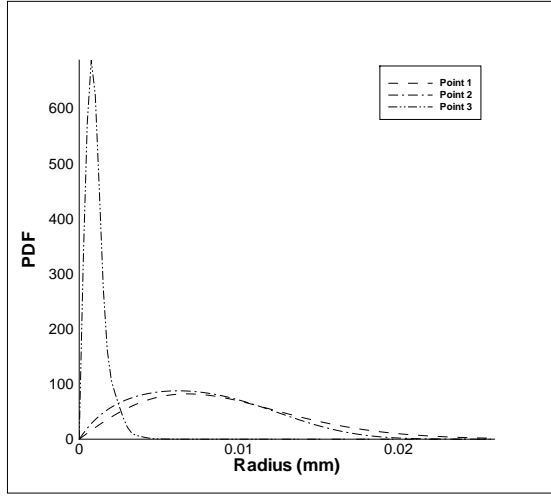


Figure 15: PDFs from the extracted moments at points 1-3

The first method is presented in Fig. 16 at points 1-3 for a range of exponent values (0.2, 0.4 and 0.6). The index i in Eq. (20) is set as 3. At points 1 and 2, very similar shaped velocity profiles are found since the underlying PDFs are similar and the difference between the continuum and spray velocity at both points is also similar. For the third point, where the underlying PDF has strong positive skew, the droplet velocity picks up slower for the small droplets compared with the droplet velocities at points 1 and 2. For large exponents ($b \geq 0.4$) the velocity profile shows exaggerated values for the larger droplet size range compared with the corresponding moment-averaged velocities listed in Table 4.

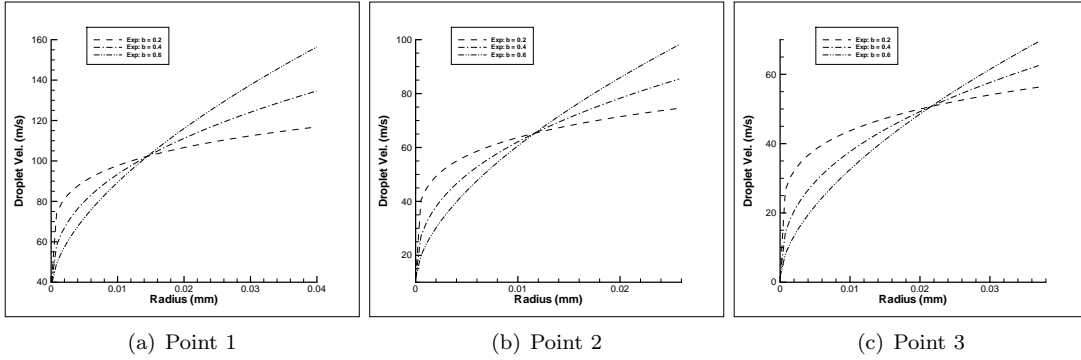


Figure 16: Droplet velocity profile based on the exponential function

The exponential function has one free parameter, the exponent, b . To obtain a uniform distribution $b = 0$, and for a linear distribution, $b = 1$. Within that range, values for the exponent are considered. Before numerical tests on the spray are performed, the behaviour of the profile is assessed based on point data from [10], along with its influence on the spray hydrodynamics models.

the effect on break-up, collision and inter-phase drag models are assessed based on data at point 1 (Table 4), whereby the source terms relate to μ_0 for break-up and collisions and $V_{d,0}$ and

$V_{d,3}$ for inter-phase drag.

The effect of varying exponent b on the hydrodynamic terms are shown in Fig. 17 for break-up and collisions and Fig. 18 for inter-phase drag.

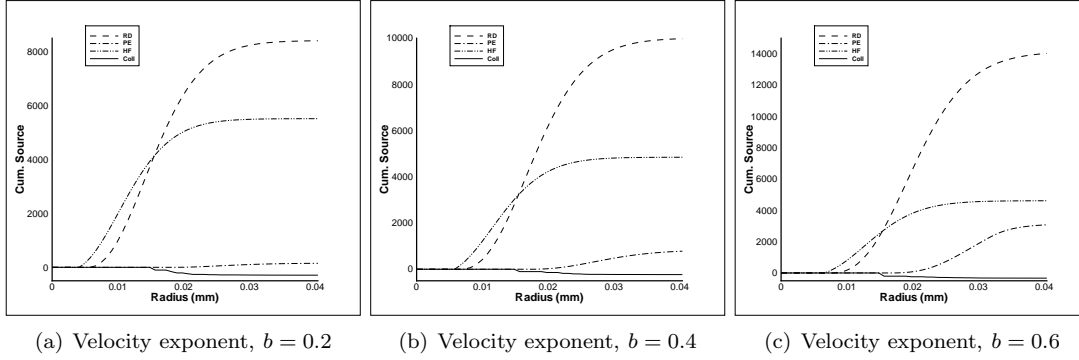


Figure 17: Cumulative break-up model terms and collision term at point 1

Of the three break-up models, HF shows virtually no change in value for the range of exponents tested, whereas both RD and PE (the selected model) do. The influence on the collision source is minimal. Comparison between the change in drag due to variation of the exponent for both the first and fourth moment highlight how spray edge SMR can be controlled to a degree. The drag source term for $V_{d,3}$ is virtually unaffected by variation in b , unlike the drag source term for $V_{d,0}$ where the magnitude is significantly reduced when the exponent is increased from 0.2 to 0.6, enabling the lower moments to convect more readily, reducing the likelihood of producing exaggerated SMR.

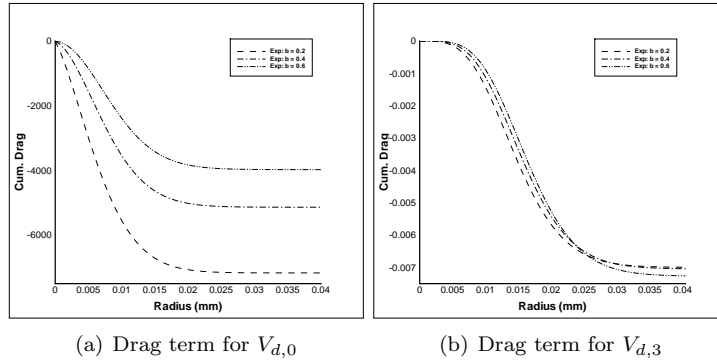


Figure 18: Cumulative drag terms at point 1

With exponents of 0.2 and 0.4, over-prediction of the leading edge SMR was found (Fig. 19(b)). Only by further increasing this value to 0.6 did the SMR drop at the front end of the spray, as shown in Fig. 19(a), thus the reference exponent is modified to 0.6. Even with such a large exponent as 0.6, the leading edge SMR does eventually pick up once the spray becomes more developed, as documented in Sect. 9.

An exponent of 0.6 tends to push up the velocity of the larger droplets beyond what is sensibly expected. Consider the data at point 1 in Table 4; the moment-averaged velocities are all around 102m/s, though Fig. 16(a) shows the constructed droplet velocity range between 40

and 160m/s, whereby the lower bound is dictated by the continuum velocity. Clearly, 160m/s is well beyond the range of the moment-averaged velocities indicating unrealistic modelling of the droplet velocities. However, at present this is the only working configuration and so it is used.

The effective upper limit of the velocity profile can be determined by looking at the associated cumulative source terms. Break-up, collision and drag models (in Fig. 17 and Fig. 18) show effectively no further contribution after 0.03mm, which corresponds to approximately 140m/s, presenting a more realistic velocity range.

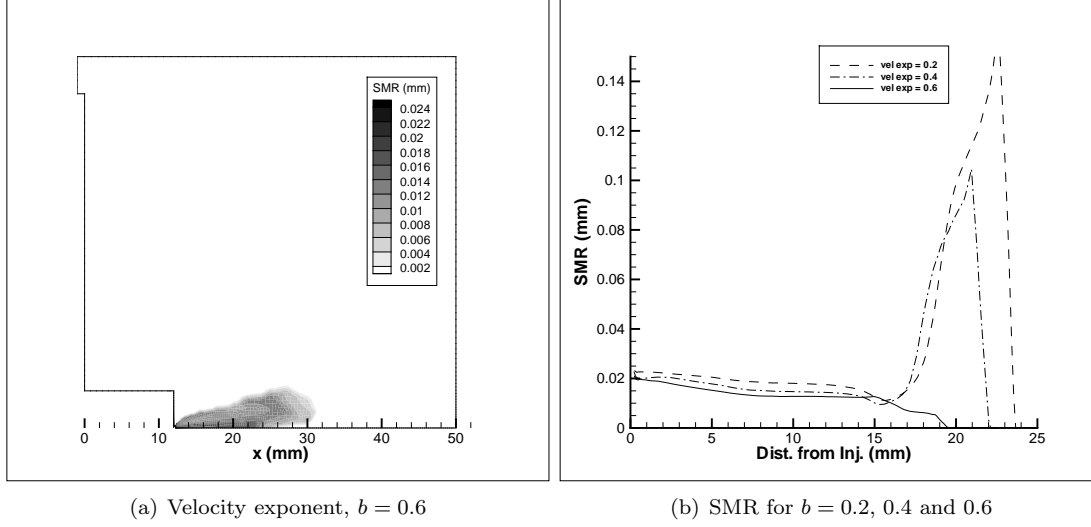


Figure 19: Variation of velocity exponent

8.5 Collisions Model

The introduction of the collisions model is expected to have the opposite effect (to some degree) on the spray compared to the break-up model. When the model is active, smaller droplets are coalescing to form larger droplets resulting in a reduction in the lower moments, manifested by an increase in the SMR. This in turn will effect the drag terms, but not to the same degree that break-up does. This behaviour is shown in Fig. 20, comparing the SMR with and without the collisions model activated.

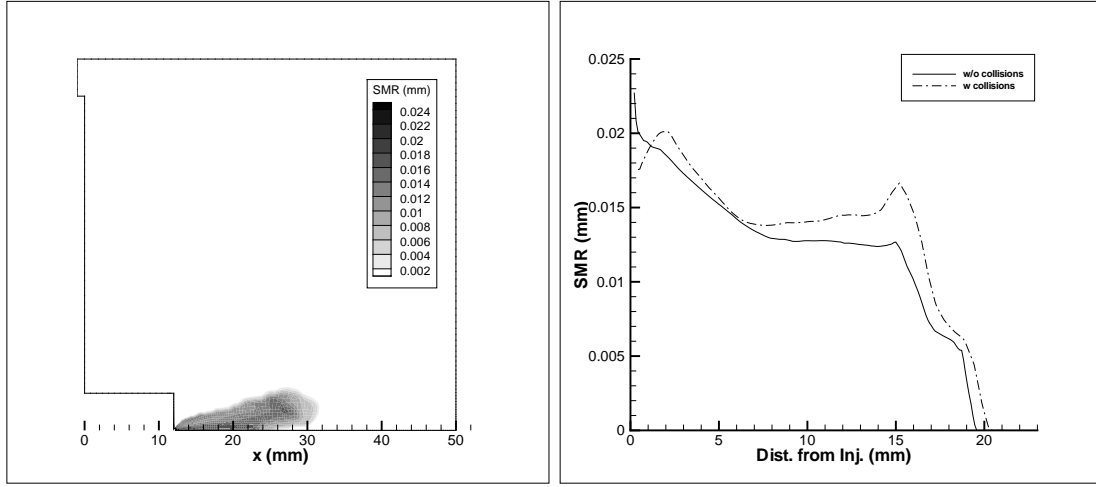
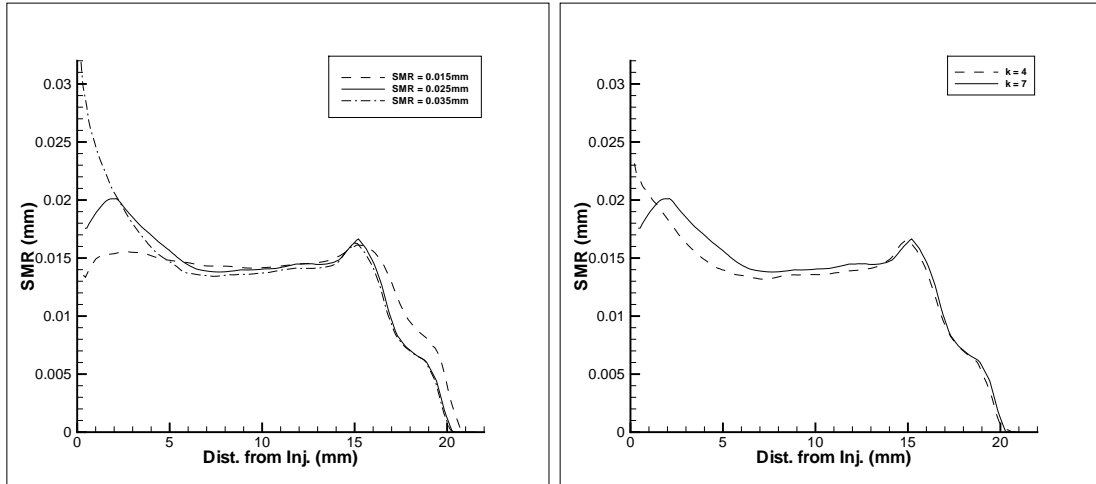


Figure 20: Activation of the collision model

From this stage the following cases include the collisions model.

8.6 Injection Parameters

As expected, neither modifying the injection SMR nor the skewness of the injected PDF had significant effect on the overall spray (Fig. 21). The only noticeable difference was that penetration was slightly increased for $r_{32,inj} = 15\mu\text{m}$. This is unusual since larger droplets retain their momentum more readily, generally causing greater penetration. This early spray development may be due to the break-up model (PE) having little effect on the spray with injection SMR of $15\mu\text{m}$, whereas for larger injection SMRs (25 and $35\mu\text{m}$) the break-up model becomes active, reducing the penetration.



(a) Variation of injection SMR

(b) Variation of injection skewness

Figure 21: Variation of injection parameters

8.7 Temporal Discretization

Time step values are based around those used by [4]. With the implementation of second order temporal interpolation, larger time steps are tested. Stability of the algorithm will be reduced with the increase of the time step, though a maximum value at which the algorithm remains stable and gives accurate results is sought.

Variation in the time step (Fig. 22(b)) shows very little difference in both the penetration and SMR, though $2\mu\text{s}$ will still be used for the calculations. Greater difference is shown between the choice of scheme (Fig. 22(a)). The penetration is noticeably different, with the Three levels discretization causing a reduction. This shows that the revision of the temporal scheme has been worthwhile.

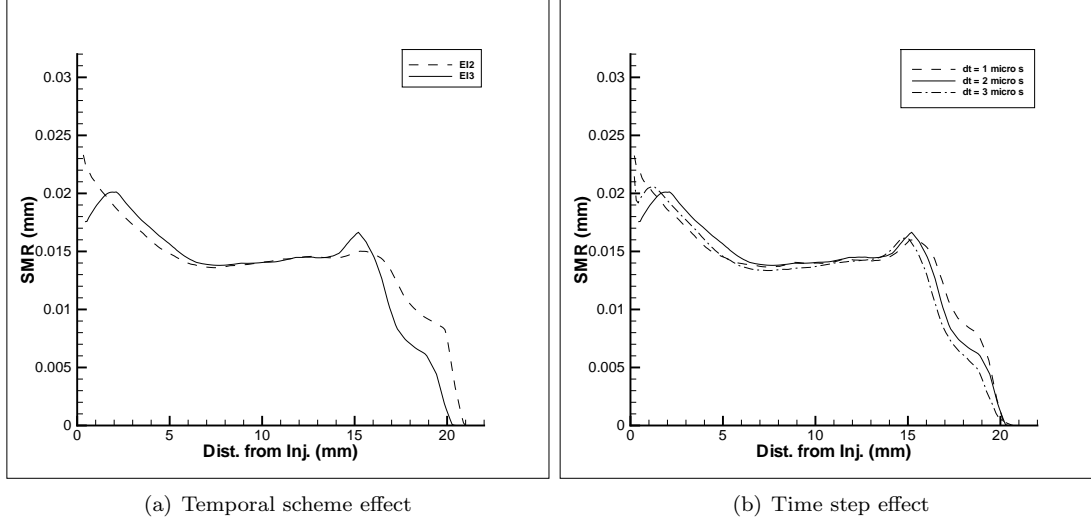


Figure 22: Variation of temporal parameters

8.8 Moments

If the Gamma distribution is used as the method of recovering the droplet size distribution, only three consecutive moments are required. Whilst any starting index is possible, the range of starting indices is chosen such that the volumetric based moment, μ_3 , is always transported. This is done so volume fractions of both phases are solved explicitly, rather than being derived from the recovered distribution, thus volume and mass concentration are more assured. Alternatively, if the Maximum Entropy distribution is used, consecutive moments from μ_0 must be transported. This means that at least four moments must be transported to include μ_3 . However, five moments must be transported to represent the main quantities used to represent a distribution (mean, variance, skewness and kurtosis).

Of the five cases listed in Table 3, the last two did not run to completion ([0 1 2 3] and [0 1 2 3 4]). The reason why comes to light when the first three cases are examined ([1 2 3], [2 3 4] and [3 4 5]). Of the first three cases (Fig. 23) the last two show strong resemblance, whereas the first case shows a huge increase in SMR at the leading edge of the spray. This shows that as lower moments are transported, the accuracy of the model degrades. The droplet velocity profile has already been shown to have a significant effect on the lower moment drag terms (Fig. 18) whereas for higher moment velocities, the shape of the profile causes only minor differences in the inter-phase

drag. Unless the droplet velocity profile is accurately represented, divergence between low order moments is likely to occur resulting in the over-estimation of SMR found in Fig. 23 and in the first two cases referred to above.

From the comparison of the first three cases, the reference transported moments are revised, becoming μ_3 , μ_4 and μ_5 , based on the trend that the further away from low order moments, the more stable the algorithm will be.

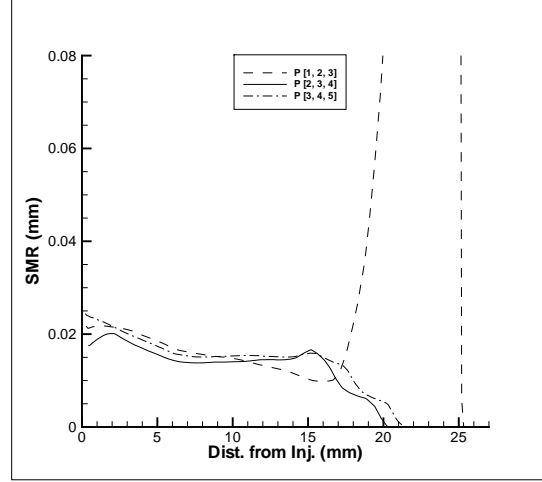


Figure 23: Choice of moments for the Gamma distribution

8.9 Parameters

The revised default parameters and submodels options are listed in Table 5. Of the nine parameters tested across their ranges (Table 3), varying four of them caused the spray model to diverge for some values (convection blending, break-up models, velocity exponent and moments). Of these four parameters, all of them are considered as key parameters in the spray model.

Table 5: Revised parameters and submodels

Parameter/submodel	Option
Moments conv. bl. (HRIC)	0.6
Velocity conv. bl. (TVD: Min-mod)	0
Break-up model	PE
velocity exponent, b	0.6
Collision model	On
SMR at injector, $r_{32,inj}$ (μm)	25
Skewness of inj. PDF, k_{inj}	7
Temporal sch.	EI3
Time step, Δt (μs)	2
moments, $P_\mu[-]$	[3 4 5]

From the list of revised parameters, a final case is run whereby the geometry is modified to allow the spray to propagate freely, and the runtime is extended to two milliseconds. This

test aims to show whether the spray calculations remain stable over long durations and to show whether the SMR remains at a sensible level.

The grid used for this case is shown in Fig. 24.

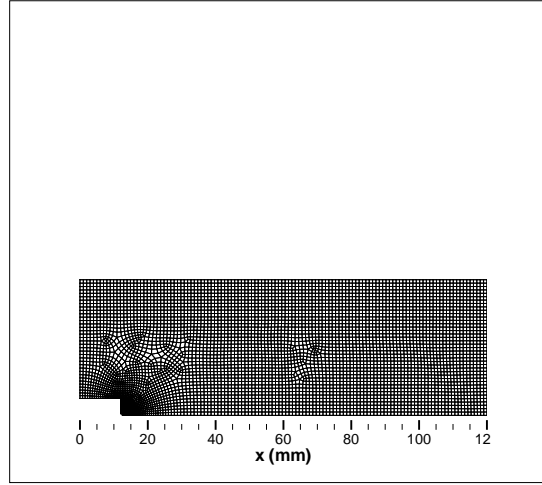


Figure 24: Computational domain for open-ended case (5271 CVs)

The results revealed that whilst the algorithm remained stable, by 1.4ms the SMR had grown at the leading edge of the spray by over an order of magnitude from the injection SMR of $25\mu\text{m}$, as shown in Fig. 25.

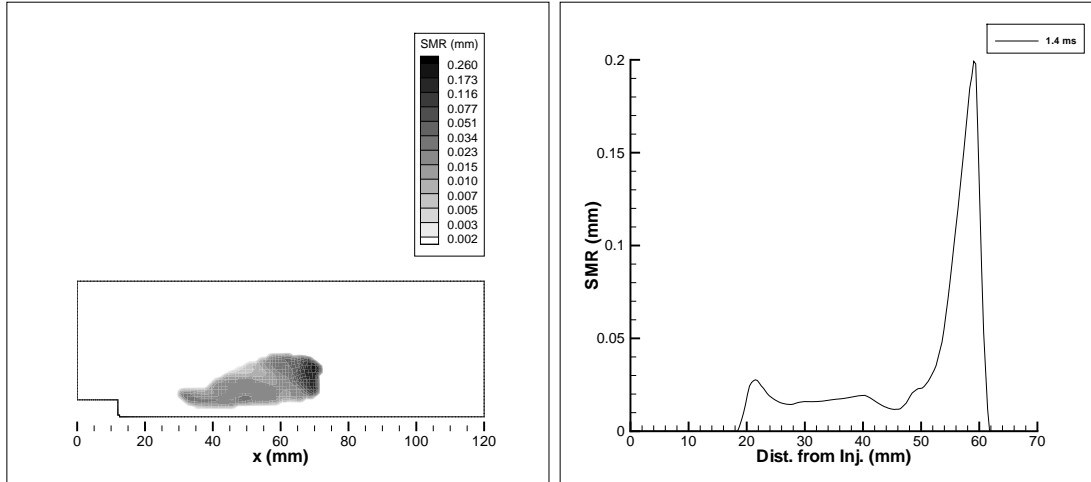


Figure 25: Sauter mean radius at 1.4ms

From this open-ended spray case and from the set of parametric cases, a preliminary conclusion can be drawn about the state of the presented spray model: the spray model becomes increasingly less accurate as it propagates. For the wall impaction case, this is not a problem since the wall prevents the spray from propagating, though for many other cases where the spray is not restricted, at present the spray model is not capable of simulating these accurately.

9 Wall Impacting Spray: Park, et al (2004)

The experimental cases of [16] were performed to present a simplified analysis of late injection stratified charge mode found in direct injection engines. The spray model developed in this work will be used to replicate one of the experimental cases computationally in order to assess its performance at both simulating the spray and modelling the spray interaction with a wall.

9.1 Case Parameters

9.1.1 Geometry

The computational grid (Fig. 26) is arranged such that the injector tip is situated 38mm in front of the wall on which the spray impacts. The narrow-cone pressure-swirl injector operating at 6.8MPa producing a nominal cone angle of 20 degrees is assumed here to have an orifice radius of 0.25mm. The injector tip is shown as a bluff-body in the bottom left-hand corner of the grid.

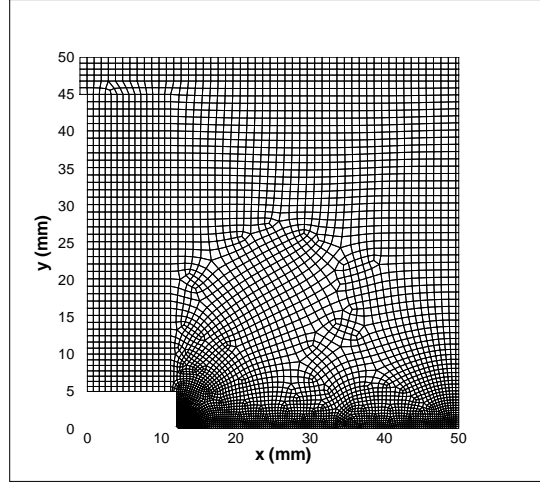


Figure 26: Computational domain for wall impaction case (5103 CVs)

Grid refinement is shown around the injector forming five injector inlet faces (Fig. 27(a)), along the line of symmetry. A relatively coarse layer of cells is found along the right hand side of the grid, where the impacting wall boundary is defined (Fig. 27(b)). This coarse layer is designed to avoid the liquid volume fraction in the near-wall cells becoming over-full. Finally, the protrusion at the top left hand corner of the grid is the outlet, situated far away from the spray. The outlet is necessary in this case since the flow is assumed to be incompressible.

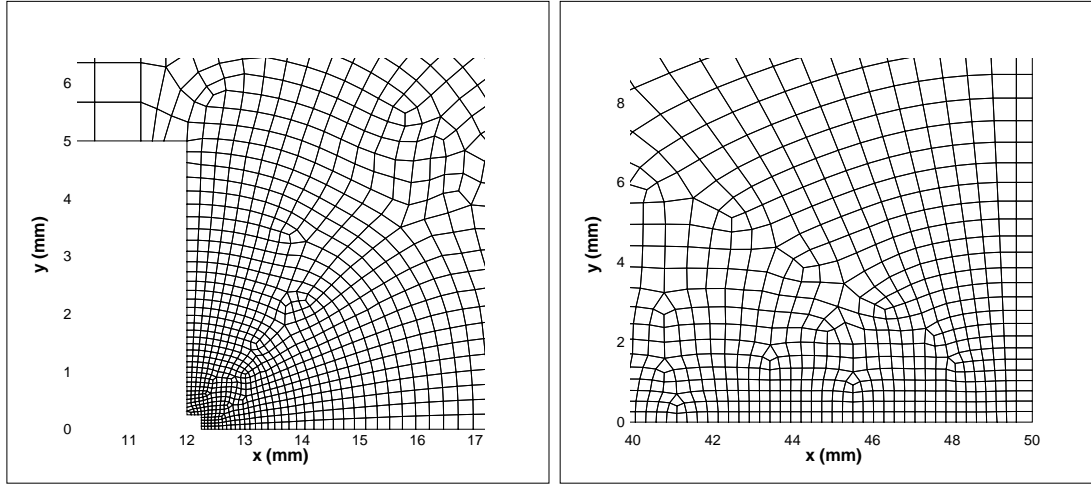


Figure 27: Injector and wall treatment

No grid independence testing is given here for two reasons. First, the grid presented is finer (in the areas of interest) than the grids used by [5, 12]. In their grids, the injector was resolved with a maximum of three cells. Secondly, this is as fine a grid as can be afforded for this study, with the algorithm taking around 8 hours to complete (spray source terms plus twenty seven partial differential equations are solved per iteration).

9.1.2 Modelling Parameters

The case is run at room temperature with an elevated pressure of 4.7kPa, giving a air density of 5.5kgm^{-3} . Molecular viscosity is taken as $1.846 \times 10^{-5} \text{kgm}^{-1}\text{s}^{-1}$. Iso-octane is the injected fuel, having a density of 702kgm^{-3} and viscosity of $5.65 \times 10^{-5} \text{kgm}^{-1}\text{s}^{-1}$. Surface tension coefficient between air and Iso-octane is 0.0226kg s^{-2} .

Injected Sauter mean radius is set as one tenth of the injector orifice radius to $25\mu\text{m}$ and the skewness parameter $k = 7$. Spray velocity and continuum velocity are assumed to be equal. Injection duration is set as 0.5ms with the injector needle rise time set as 0.025ms. This rise time is an overestimate (it should be approximately 0.01ms), but is used because divergence occurs if the injector is turned on and off too abruptly.

Droplet velocity profile exponent is set to 0.6. Both the break-up model of [17] [PE] and the collision model are employed. For determining whether the full set of moments are present in a given volume, the multiplier, C_μ , is set to 1×10^{-7} . The underlying distribution is assumed to be a Gamma distribution and the moments μ_3 , μ_4 and μ_5 are used to determine its parameters. All terms related to the PDF and velocity profile are solved using numerical integration, discretized with 30 segments. Ideally the distributions should be divided into at least forty segments, though this is not done because of the computational cost incurred.

9.1.3 Discretization

Second order Euler implicit temporal discretization [EI3] is used for all transport equations, with a constant time step of $2\mu\text{s}$. The convection discretization is detailed in table 6. No high order convection scheme is used for the moment-averaged momentum equation. Eddy viscosity is under-relaxed by the same constant used for the turbulence equations. Relatively low convection blending is used for the turbulence modelling to stabilize the algorithm.

Table 6: Discretization Parameters for wall impaction case

Transport equation	Under-relaxation	Convection blending
Continuum momentum	0.7	0.9 (TVD: Min-mod)
Continuum turbulence	0.65	0.5 (TVD: Min-mod)
Discrete momentum	0.7	0
Discrete continuity	0.7	0.6 (HRIC)

Two iterations are performed on all gradient calculations, dropping the error one order of magnitude. Further iterations of the gradient showed very little gain in accuracy. Pressure and pressure correction are interpolated from the near-boundary CVs to the boundary after the first iteration.

9.1.4 Initialization

Only the turbulent kinetic energy and dissipation rate require non-zero domain initialization. Values of these are sought such that the resulting eddy viscosity is as small as possible without causing the algorithm to diverge early in the solution procedure. Over-estimation of eddy viscosity has been found to excessively resist the acceleration of the continuum phase.

The characteristic length scale of the initial turbulence is assumed to be 1cm with a velocity of 40m/s at 20% intensity, giving initial eddy viscosity one hundred times greater than the molecular viscosity.

9.1.5 Algorithm

Outer iterations are limited to 20 and is assumed to converge once the global maximum normalized (1-norm) residual has dropped three orders of magnitude. Inner iterations (of the linear system) are required to drop the residual one order of magnitude.

9.2 Penetration and Impaction

Figure 28 from [16] shows the development and impaction of the spray, showing that impaction occurs at some time between 0.4 and 0.9ms. Cross-referencing this with the earliest recorded near-wall Weber numbers in Fig. 37 - 40, impaction is most likely to have occurred around 0.9ms after the start of injection.

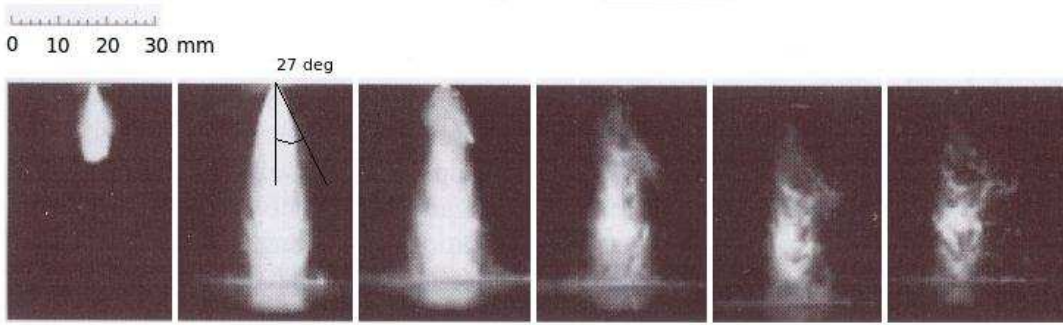


Figure 28: Spray from 0.4ms at intervals of 0.5ms

From Fig. 28 taken from [16], the spray half-cone angle is estimated as being 27 degrees. However, the cone angle is stated as being 20 degrees, implying a half-cone angle of 10 degrees. Clearly there is a discrepancy, so for the computational case a compromise is made by setting the half-cone angle to 20 degrees.

In the same figure, penetration at 0.4ms is shown to be approximately 16mm and at 0.9ms the spray reaches the wall, which is 38mm from the injector. This implies that the spray accelerates towards the wall, which is highly unlikely. A more likely explanation is that the first image in Fig. 28 corresponds to an earlier time. Comparing the first two images in Fig. 28 with the profiles in Fig. 29, good correlation of the spray shape is found at 0.9ms, especially at the front end of the spray. The experimental case shows a greater degree of spreading as the spray exits the nozzle, causing greater retardation to the spray than in the computational case.

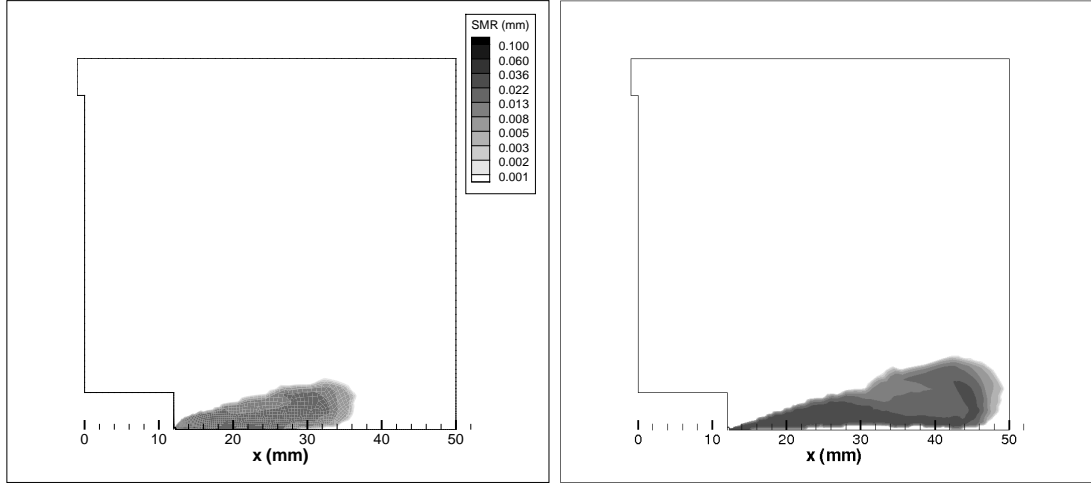


Figure 29: Sauter mean radius at 0.4 and 0.9ms

Early spreading of the spray outwards is strongly resisted by the gas phase as it is drawn towards the injector orifice by the sharp drop in pressure in that region, forming a small vortex just in front of the nozzle (Fig. 30).

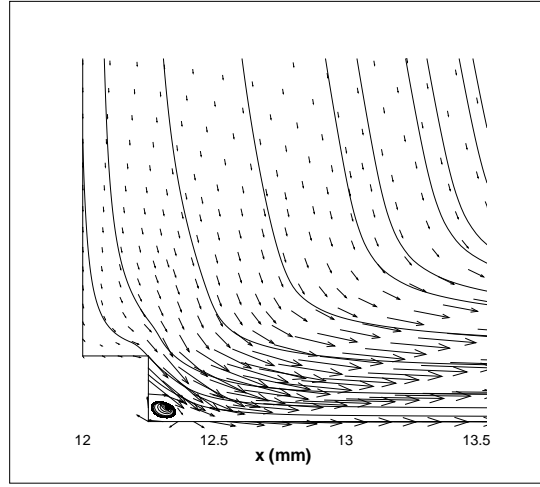


Figure 30: Near-nozzle flow of the surrounding gas (at 0.4ms)

The penetration rate of the spray model shown in Fig. 31 appears to be accurate, gradually slowing down as the spray progresses with spray tip arriving at the wall by 0.9ms, which is the initial impaction time recorded by [16].

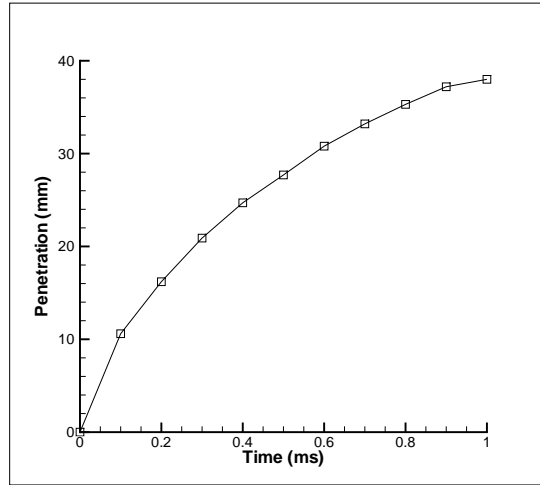


Figure 31: Penetration rate of the spray model

Although the injector pulse width is only 0.5ms, at both 0.9 and 1.4ms there still appears in Fig. 28 to be a strong concentration of the spray from the injector tip, appearing as though the injector is still spraying. This is also found in the computational results, as shown in Fig. 29 - 34, but with a reduced spray width at the tail-end of the spray. (At 10mm from the injector at 0.9 and 1.4ms the spray width is 9mm and 8mm respectively, whereas the computational results show half-thicknesses of 3mm and 2mm, respectively.)

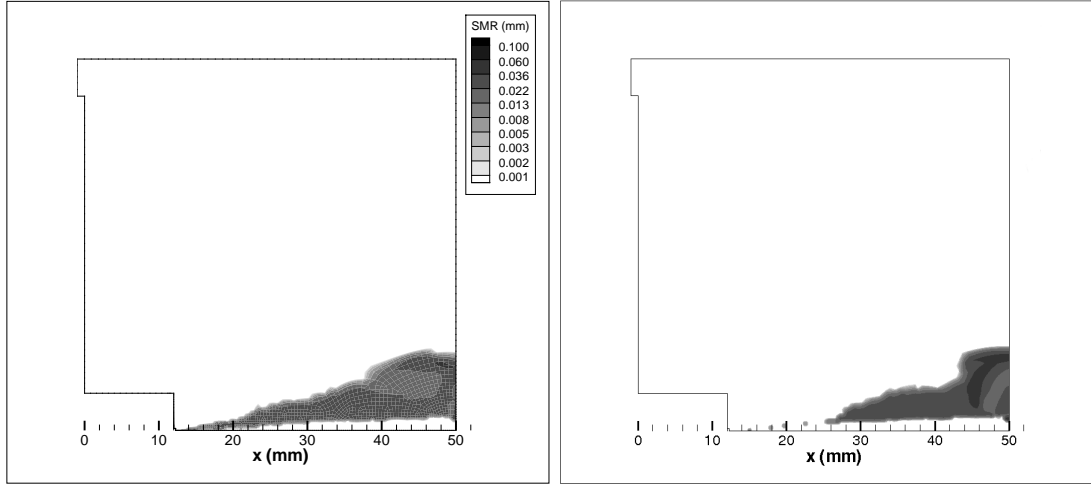
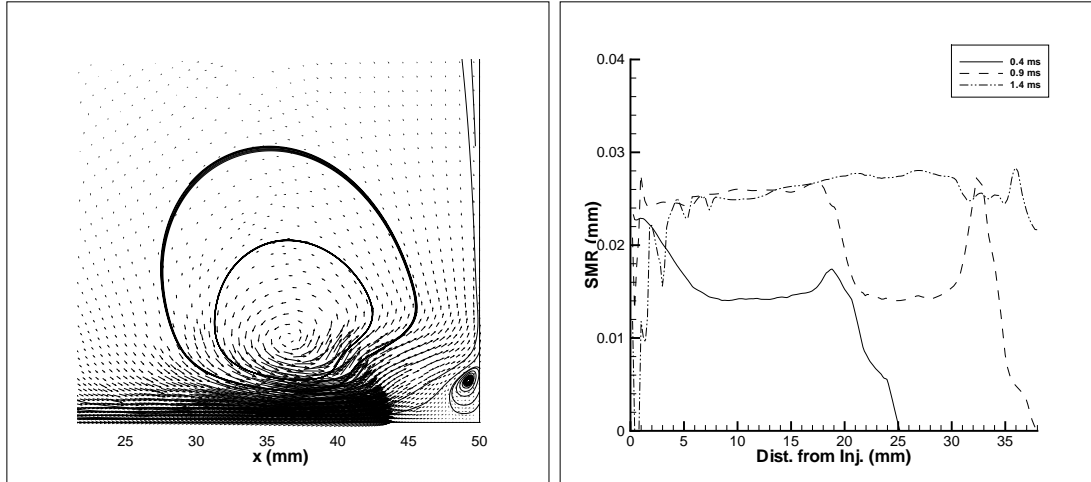


Figure 32: Sauter mean radius at 1.4 and 1.9ms

The contraction of the spray is attributed to the effect the continuum has on these trailing droplets. Figure 33(a) shows how the gas phase velocity forms an anti-clockwise vortex, which pushes the upstream spray towards the centreline resulting in a smaller SMR along the chordline (Fig. 33(b)) and pulls the downstream spray outwards.



(a) Anti-clockwise vortex formed in the gas phase (at 1.2ms)

(b) SMR along the chordline from 0.4ms to 1.4ms

Figure 33: Effect of the gas flow on the spray

Only after 1.9ms does the spray concentration drop downstream of the injector. This pattern of the spray development indicates that the trailing edge of the spray after injection is completed is being carried by the surrounding gas. This retardation of the trailing edge of the spray was also found in the computational model, as shown in Fig. 32 - 34.

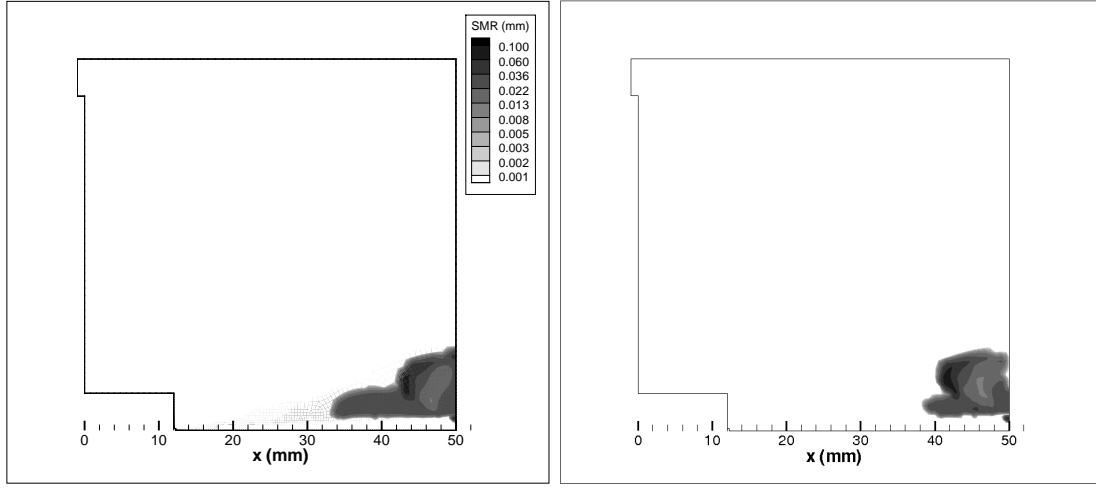


Figure 34: Sauter mean radius at 2.4 and 2.9ms

Chordline values of volume weighted SMR show the drop in mean radius near the wall due to the break-up of splashing droplets. Further out from the wall the SMR picks up because the splashing droplet distribution is strongly positively skewed.

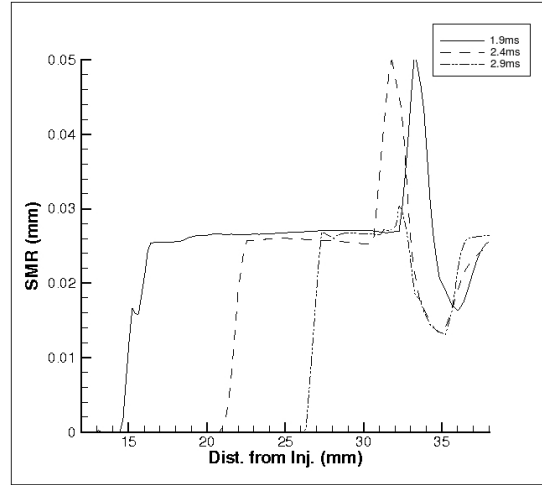


Figure 35: Sauter mean radius along the chordline from 1.9ms to 2.9ms

9.3 Near-wall Weber Number

The droplet Weber number

$$We_d = \frac{2r \rho_d V_{d,n}^2}{\sigma_d} \quad (75)$$

is sampled at locations in front of the wall, as shown in Fig. 36. Line *abc* is 1mm above the wall, line *def* is 3mm above the wall and lines *ad*, *be* and *cf*, are 0, 4 and 8mm from the centreline.

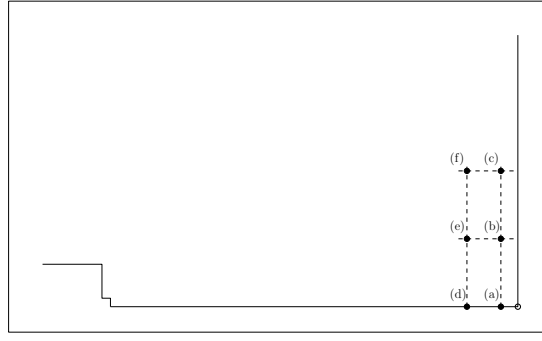


Figure 36: Sampled Weber number locations

Pre-impingement Weber numbers at each location were measured with respect to time and are plotted in Fig. 37 - 40, showing both the experimental data and the computational data where the spray was present. In [16] it is stated that the near-wall drop radii were in the range of 2 to 50 μm and the normal droplet velocity component was less than 15m/s. Computational data showed substantial over-prediction of the droplet velocity (with the largest value of 27m/s), which when squared in the calculation of the Weber number, further magnifies the error.

With the impinging droplets having such momentum, the post-impingement droplets will tend to have sufficient momentum to overcome the cross-flow of the gas phase, resulting in the droplets penetrating into the oncoming spray rather than being carried radially outward over the wall.

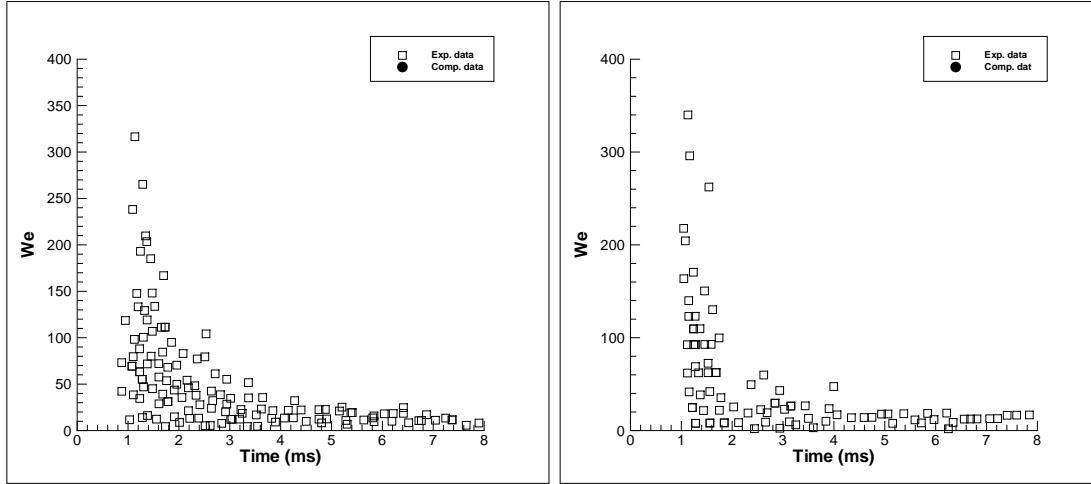


Figure 37: Weber number before impaction at positions (a) and (d)

Since the spray form was assumed to be a hollow cone shape in the computation, no centreline data exists in front of the wall (Fig. 37). However, experimental data shows a very clear presence of droplets heading towards the wall along the centreline. This indicates that the spray should have been modelled to consider the pre-swirl injection stage, as discussed in [24] (though details about the transient behaviour of the process in this case are lacking), whereby fuel initially exits the nozzle along the centreline as the injector needle opens and develops into a hollow cone as the spray gains swirl momentum (Fig. 38).



Figure 38: Pre-swirl injection stage [24]

Four millimetres out from the centreline, the difference between the spray and the computational model are shown in Fig. 39. Initial over-prediction of the Weber number does decay rapidly with time, though by 4ms the entire injected spray has interacted with the wall.

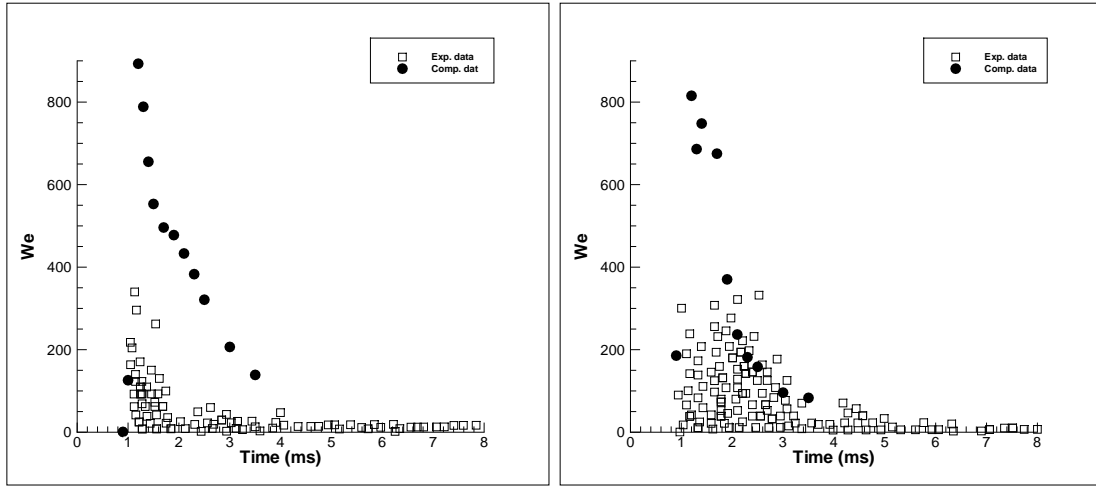


Figure 39: Weber number before impaction at positions (b) and (e)

At the outer edge of the spray, the Weber numbers of the computation model remain high, whereas the experimental data shows decaying Weber numbers away from the centreline.

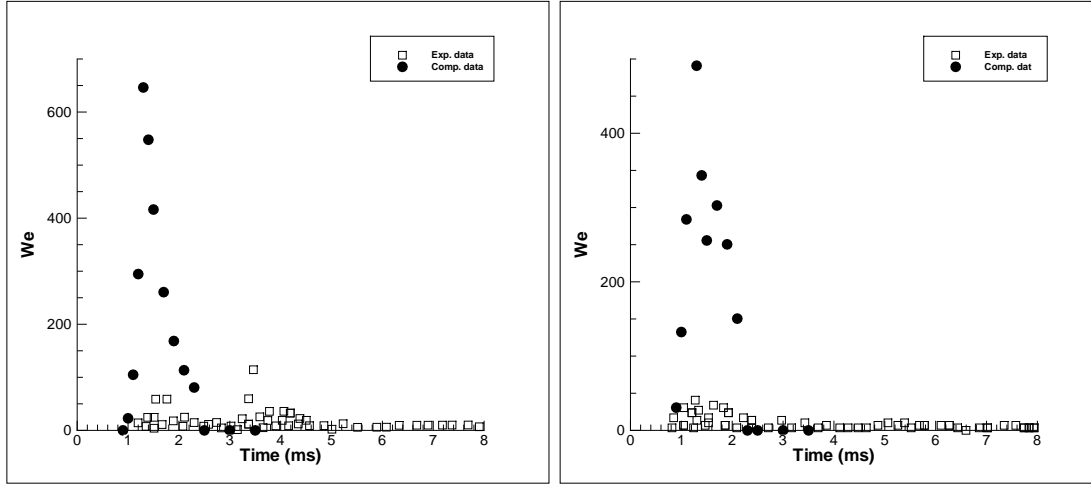


Figure 40: Weber number before impactation at positions (c) and (f)

Post-impingement Weber numbers are shown in Fig. 41, where the experimental data is taken at the centreline position (a) and the computational data is taken at position (b) because no data exists for position (a) . The computational model shows that droplets rebound immediately after the spray begins to impact on the surface, whereas in the experimental case this only occurs after 3ms, implying that droplets prior to this time stuck to the surface, forming a film of liquid. Once the film is formed, rebounding readily occurs for droplets with low Weber numbers ($We < 5$).

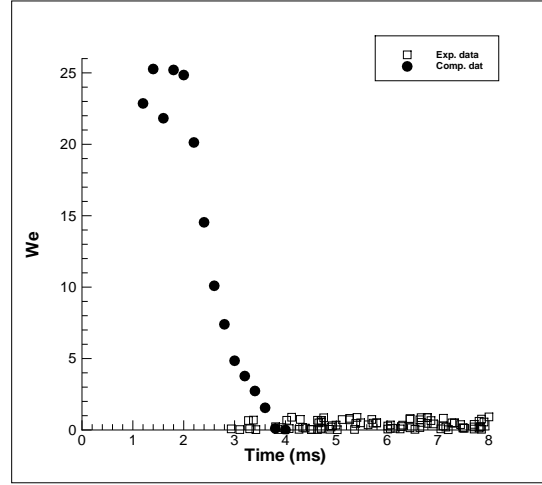


Figure 41: Weber number before and after impactation at position (a)

9.4 Wall Wetting

The wetted patch from the experimental results has a radius of approximately 11mm, which compares reasonably well with the wetted footprint produced by the model, shown in Fig. 42.

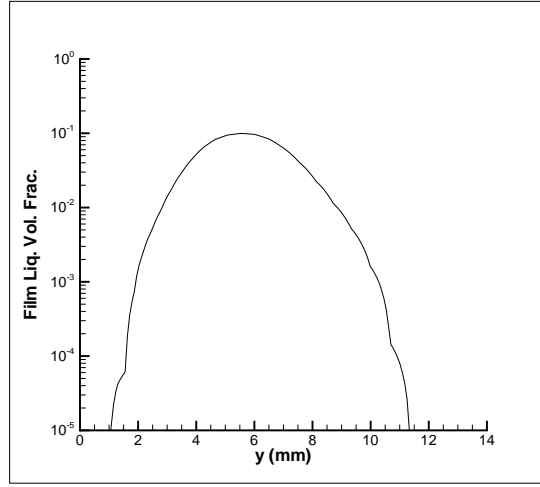


Figure 42: Near-wall liquid volume fraction

9.5 Discussion

The complete spray model operating with optimal parameters shows that the current implementation is capable of simulating spray propagation and wall interaction to a reasonable degree of accuracy. The poor accuracy found in the comparison of near-wall Weber numbers is likely to be associated with the parameters set for the injection conditions, particularly the half-cone angle.

Further simulations were run with wider half-cone angles (25 and 30 degrees) though neither case ran to completion due to numerical divergence after 0.7ms. The cause of divergence is likely to be related to the increased effect of drag on the spray causing greater differentiation of the moments, leading to over-estimation of the SMR. These tests were attempted based on the assumption that as the cone angle is increased, near-wall droplet velocity would drop, bringing the Weber numbers more in line with the experimental data.

Further experimental comparisons with the spray model are not documented in this section since the parametric tests earlier in this chapter showed that the model is still in a substandard condition. Until the problematic parametric cases are re-addressed and corrected and the model is shown to be robust, such comparisons are considered to be of limited use.

10 Conclusion

Despite the capacity that the Maximum Entropy formalism has for constructing accurate distributions, its incorporation into the spray model presented no benefit. This is not due to the method itself, but to the apparently divergent nature of the current formulation of the spray model.

Although the revised droplet velocity profile did not characterize the droplet velocity accurately enough to allow the lower moments to be transported properly, it provides sufficient improvement to enable the full spray model to be run using high order moments. Varying the exponent showed how significantly the velocity distribution effects the characteristics of the spray, indicating how important it is to ensure the profile is estimated accurately.

The hydrodynamic contributions are generally over-estimated for the lower order moments (such as the inter-phase drag) which is due to either the droplet size distribution being too strongly positively skewed and/or the droplet velocity profile over-estimating the difference between the velocity of the smaller droplets and the velocity of the surrounding gas. An attempt to minimize this difference could be performed by prescribing certain conditions of the velocity profile, such as its derivative must be equal to zero at the limits of the profile.

High order convection schemes for all transport equations were implemented. The lack of such schemes was a major shortcoming in both the works of [3] and [12] and those authors acknowledged the need to address this. Two new schemes were implemented; the TVD scheme for the velocities and turbulence models and HRIC scheme for the moments. The use of the HRIC scheme had the most significant effect on the spray, enabling clearer resolution of the hollow cone spray structure. Implementation of the Three time levels method for approximating the temporal terms show noticeable, though not considerable, difference in the spray compared to the Euler implicit scheme used by [3].

A suitable wall impaction model was implemented successfully to the spray model which retains as much detail of the rebounding and splashing sprays as the impinging spray, enabling coexistence of all three sprays within a given volume. The model has been shown to work successfully, transitioning the impaction conditions from dry to wet with the data obtained from the liquid film equation.

References

- [1] M. Ahmadi and R. W. Sellens. A simplified maximum-entropy-based drop size distribution. *Atomization and Sprays*, 3:291–310, 1993.
- [2] C. Bai and A. D. Gosman. Development of methodology for spray impingement simulation. *SAE Technical Paper Series*, (950283), 1995.
- [3] J. C. Beck. *Computational modelling of polydisperse sprays without segregation into droplet size classes*. Ph. D. Thesis, UMIST, 2000.
- [4] J. C. Beck and A. P. Watkins. On the development of spray submodels based on droplet size moments. *J. of Comp. Phys.*, 182:586–621, 2002.
- [5] J. C. Beck and A. P. Watkins. On the development of a spray model based on drop-size moments. *Proc. R. Soc. Lond.*, A(459):1365–1394, 2003.
- [6] C. T. Crowe, M. Sommerfeld, and Y. Tsuji. *Multiphase Flows with Droplets and Particles*. CRC Press, 1998.
- [7] R. O. Grover and D. N. Assanis. A spray wall impingement model based upon conservation principles. *The Fifth International Symposium on Diagnostics and Modeling of Combustion in Internal Combustion Engines*, 2001.
- [8] L. P. Hsiang and G. M. Faeth. Near-limit drop deformation and secondary breakup. *Int. J. Multiphase Flow*, 18(5):635–652, 1992.
- [9] V. John, I. Angelov, A. A. Oncul, and D. Thevenin. Techniques for the reconstruction of a distribution from a finite number of its moments. *Chemical Engineering Science*, 62:2890–2904, 2007.

- [10] D. P. Jones and A. P. Watkins. Droplet size and velocity distributions for spray modelling. *Journal of Computational Physics*, 2011. accepted.
- [11] E. Lemini and A. P. Watkins. Development of a spray wall impaction model without discretisation into droplet size classes. *ILASS-Europe 2002*, 2002.
- [12] E. E. Lemini. *A new methodology for modelling impinging sprays based on drop size moments*. Ph. D. Thesis, UMIST, 2004.
- [13] S. Muzaferija and M. Peric. Computation of free-surface flows using interface tracking and interface-capturing methods. *Non-linear Water Wave Interaction*, pages 59–100, 1999.
- [14] J. A. Nicholls. Stream and droplet breakup by shock waves. in *NASA SP194 (Eds. D.T. Harrie and F.H. Reardon)*, pages 126–128, 1972.
- [15] P.J. O'Rourke. *Collective Drop Effects on Vaporising Liquid Sprays*. PhD Thesis, University of Princeton, 1981.
- [16] J. S. Park, H. S. Kim, and M. C. Lai. Visualization and measurement of a narrow-cone di gasoline spray for the impingement analysis. *Int. J. of Automotive Technology*, 5(4):221–238, 2004.
- [17] M. Pilch and C. A. Erdman. Use of breakup time data and velocity history data to predict the maximum size of stable fragments for acceleration-induced breakup of a liquid drop. *Int. J. Multiphase Flow*, 13(6):741–757, 1987.
- [18] R. D. Reitz and R. Diwakar. Effect of drop breakup on fuel sprays. *SAE Technical Paper Series*, (860469), 1986.
- [19] D. W. Stanton and C. J. Rutland. Multi-dimensional modeling of heat and mass transfer of fuel films resulting from impinging sprays. *SAE Paper*, (980132), 1998.
- [20] A. Tagliani. Numerical aspects of finite Hausdorff moment problem by maximum entropy approach. *Applied Mathematics and Computation*, 118:133–149, 2001.
- [21] G. Talenti. Recovering a function from a finite number of moments. *Inverse Problems*, 3:501–517, 1987.
- [22] H. K. Versteeg and W. Malalasekera. *An Introduction to Computational Fluid Dynamics*. Pearson, second edition, 2006.
- [23] A. P. Watkins. Modelling the mean temperatures used for calculating heat and mass transfer in sprays. *International Journal of Heat and Fluid Flow*, 2006.
- [24] G. Wigley, G. Pitcher, D. Law, B. Schneider, and S. Rogers. Effect of compression pressure on the spray morphology of gdi pressure-swirl injectors. *The Fifth International Symposium on Diagnostics and Modeling of Combustion in Internal Combustion Engines*, 2001.
- [25] A. D. Woodbury. A Fortran program to produce minimum relative entropy distributions. *Computers and Geosciences*, 30:131–138, 2004.
- [26] B. Yue and A. P. Watkins. Mathematical development and numerical analysis of further transport equations for the droplet size moment theory. *19th Annual Meeting of the Institute for Liquid Atomization and Spraying Systems (Europe)*, 2004.